CHALMERS
UNIVERSITY OF TECHNOLOGY

Monte Carlo Simulation of GaAs Schottky Barrier Diodes for THz Applications

Master's thesis in Wireless, photonics and space engineering, MSc

XENIA LÖÖV

DEPARTMENT OF MICROTECHNOLOGY AND NANOSCIENCE

CHALMERS UNIVERSITY OF TECHNOLOGY
Gothenburg, Sweden 2026
www.chalmers.se

Monte Carlo Simulation of GaAs Schottky Barrier Diodes for THz Applications
Xenia Lööv

Masters thesis, 2026
Department of Microtechnology
Terahertz and Millimetre-wave Laboratory
Chalmers University of Technology

Supervisor: Helena Rodilla
Examiner: Jan Stake

This thesis is typeset using **typst**.
All simulation code is written in the *Rust* programming language.
All data processing is done in *Python* and all plots are generated using *matplotlib*.
Absolutely no Artificial Intelligence (AI) or Large Language Model (LLM) tools were used in any form to assist with the creation of this thesis.

Monte Carlo Simulation of GaAs Schottky Barrier Diodes for THz Applications
Xenia Lööv
Chalmers University of Technology

Abstract

Accurate models for GaAs Schottky barrier diodes are essential for implementing room-temperature mixers and frequency multipliers for use in the terahertz range. Increased electron temperatures by the Schottky contact and effects from intervalley scattering make traditional drift-diffusion methods unsuitable for simulating such devices. This work implements a Monte Carlo simulator based on a microscopic model for electron transport in GaAs. A three-valley (Γ, L and X) spherical non-parabolic band structure is assumed, and impurity, optical phonon and acoustic phonon scattering mechanisms are considered for the model. Homogeneous (bulk) transport properties of GaAs are simulated, showing good agreement with published values of mobility and diffusion coefficient versus field strengths, accurately predicting the critical field and saturation velocity for the carriers as they enter heavier valleys. The simulator is also used to simulate a number of Schottky barrier diodes fabricated at Chalmers University of Technology. The results show good agreement with the measured IV-characteristics, with the ideality factor being within 10% and saturation current within a factor of 3. The voltage-capacitance relationships agree well with the ideal diode model, the zero-voltage capacitance being within a few percent. The simulation shows an increased carrier temperature at the Schottky contact at higher currents, consistent with previous results, indicating an increased noise temperature at higher currents.

Keywords: semiconductor simulations, Monte Carlo, Schottky barrier diode, GaAs

Contents

1. Introduction

The THz frequency region, typically defined between 100 GHz to 10 THz, is a region with many scientific uses, but has largely been driven applications in radio astronomy and atmospheric science [1]. While ground-based radio astranomical telescopes typically use cryogenically cooled semiconductor-insulator-semiconductor (SIS)-mixers or hot electron bolometer (HEB)-mixers, providing the lowest possible noise temperature, in many applications such as space-borne missions or lower cost atmospheric measument missions, cryogenic cooling is either not available, impractical or too costly. In such applications, GaAs Schottky barrier diode mixers are typically used [2] due to its large bandgap leading to low leakage currents and high mobility leading to a low series resistance [3]. Additionally, the local oscillator feeding the mixers typically utilize GaAs Schottky barrier diodes for frequency multiplication into the THz region [2].

There are a number of space-borne radio telescopes operating in the THz area. The Swedish *Odin* satellite operating between 486-580 GHz, NASA's *Microwave Limb Sounder* (MLS) operating between 118 - 2520 GHz and the *Herschel Space Observatory* which operated between 480 - 1910 GHz. In the first two, cryogenic cooling is not available and Schottky barrier diodes are used for mixing. In the *Herschel Space Observatory*, cryogenic cooling was available and SIS- and HEB-mixers were used depending on the channel, with Schottky barrier diodes used in the frequency multiplier stages for the local oscillator signal feeding the mixers [1].

In a Schottky barrier diode mixer, the frequency range of operation and the efficiency of a Schottky barrier diode is tied to the parasitic capacitance and the series resistance of the diode [4]. For high-performance mixers in the THz region, accurate modelling of these parameters, as well as the IV-characteristics of the diode is exceedingly important. Therefore, accurate models that can predict the characteristics of a diode without having to fabricate and measure the device are of great importance. Additionally, the Schottky barrier diode mixer is typically the limiting component in a receiver in terms of noise. Therefore, accurately modelling the noise characteristics of a diode is of importance when designing Schottky barrier diode based mixers [5]. In Schottky barrier diode, the regular thermal (Johnson) noise and shot noise are present, but other effects are also present: at high fields, the energy of the electrons increase beyond that of the thermal energy at the lattice temperature. These "hot electrons" cause additional noise higher than what would be predicted by the thermal and shot noise alone [6]. Additionally, at high electron energies, intervalley scattering causes fluctuations in velocity leading to noise at high depletion region fields [7].

Multiple methods exist for approximating solutions to the Boltzmann transport equation, the equation governing the charge transport in semiconductors: the

Drift-Diffusion (DD) and Hydrodynamic (HD) methods are based on different moments of the equation. However, these methods typically rely on approximations for different aspects of the behaviour of the electrons. The distribution function for velocity is typically taken as a Maxwell-Boltzmann distribution, and the relation between the velocity of the carriers and the local electric field is often assumed static in time. As such, these methods generally struggle with treating effects such as velocity overshoot, non-maxwellian carrier distributions and carrier inertia, and often are limited in describing the details of the scatter events in the semiconductor, typically relying on energy-dependent relaxations times [5].

The Monte Carlo method applied to semiconductor simulations, introduced by Kurosawa at the Kyoto Semiconductor Conference in 1966 [8], later refined by Rees [9] and Fawcett [10], is instead based on the microscopic model of individual electrons interacting with the semiconductor lattice. From its microscopic rather than macroscopic nature, it provides more accurate results applicable to higher frequencies than the previously mentioned methods. As each individual electron is simulated, no assumptions need to be made about the distribution function of electrons. Additionally, the scatter events can be described in terms of a probability distribution of scattering between different states, rather than being described only by (energy-dependent) relaxation times, meaning the scatter events can be more accurately modelled [11].

In this work, a Monte Carlo simulator for simulating GaAs Schottky barrier diodes is implemented. The diodes simulated were dimensioned to match a number of GaAs Schottky barrier diodes for use at THz-frequencies, manufacted at the Terahertz and Millimetre-Wave Laboratory at Chalmers University of Technology. The results of the simulator are compared against those measured for the manufactured diodes.

2. Theory

In this section, a microscopic model of electrons in semiconductors is described in Section 2.1 and Section 2.2. The microscopic model is applicable to most semiconductors, but in this work it is described as it applies specifically to GaAs. In Section 2.3 the thermionic emission theory is described for the Schottky barrier diode.

2.1. Electrons in semiconductors

Most semiconductors are crystalline solid materials, i.e. a lattice of atoms with translational symmetry along a number of lattice vectors $\vec{a}_i$. This work is concerned with gallium arsenide (GaAs), a semiconductor crystal with a double face-centered cubic structure (a Zinc-Blende crystal structure) as shown in Figure 1.

As the semiconductor forms a lattice, its quantum mechanical potential is periodic, $\mathbb{V}(\vec{r}) = \mathbb{V}(\vec{r} + \vec{a}_i)$. From Bloch's theorem [12], electrons are divided into a number of energy bands, where each electron is described by a lattice-periodic Bloch function $u(\vec{r}) = u(\vec{r} + \vec{a}_i)$ modulated by a plane wave with wave vector $\vec{k}$ forming its wave function

$$\psi_{n,\vec{k}}(\vec{r}) = u_n(\vec{r}) \exp\left(-j\vec{k} \cdot \vec{r}\right) \tag{1}$$

where n is the band the electron belongs to and j is the imaginary unit.

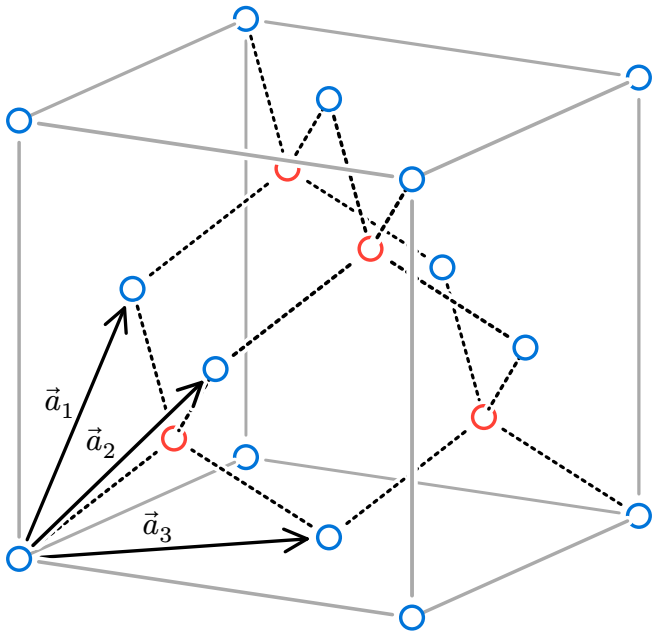

Figure 1: Crystalline structure of GaAs. Gallium atoms are marked in blue, arsenide in red. Chemical bonds are dotted lines and primitive lattice vectors $\vec{a}_i$ are marked in black.

For this set of lattice vectors $\vec{a}_i$, there exists lattice of "reciprocal vectors" $\vec{A}_j$ with the property that $\vec{A}_j \cdot \vec{a}_i$ is a multiple of 2π. For an electron with wave vector $\vec{k} + \vec{A}_j$, we note that

$$\begin{aligned} \psi_{n,\vec{k}+\vec{A}}(\vec{r}) &= u_n(\vec{r}) \underbrace{\exp\left(-j\vec{A}\cdot\vec{r}\right)}_{\text{periodic in lattice}} \exp\left(-j\vec{k}\cdot\vec{r}\right) = \\ &= \psi'_{n,\vec{k}}(\vec{r}) \end{aligned} \tag{2}$$

and the electron can be considered equivalent to an electron with wave vector $\vec{k}$. In the space of wave-vectors $\vec{k}$, the smallest volume containing all non-equivalent vectors is called the "Brillouin zone" [12]. For the FCC lattice, the Brillouin zone is a truncated octahedron, shown in Figure 2.

The energy for electrons in all bands is shown in a band structure diagram in Figure 3. $\vec{k}$ is drawn along a number of crystallographic lines marked in Figure 2, chosen to cross certain local minima of energy in the conduction band. These lines and points are:

- Γ^6 the center of the Brillouin zone, at $\vec{k} = \vec{0}$
- L^6 the center of a hexagonal face, at $k_{x,y,z} = \pm\frac{\pi}{2}a^{-1}$, with 4 equivalent points.
- X^6 the center of a square face, at $\vec{k} = (\pm\pi a^{-1}, 0, 0)$ and all permutations, with 3 equivalent points.
- Λ the line between Γ^6 and L^6
- Δ the line between Γ^6 and X^6

In this work, the Γ^6-, L^6- and X^6-valleys will be referred to as the Γ-, L- and X -valleys respectively for brevity.

At zero temperature, the electrons in a semiconductor will fill all bands up to a certain energy level. The highest band fully filled by electrons at zero temperature is called the valence band, and the lowest energy band empty of electrons is called the conduction band [8], both shown in Figure 3. At non-zero temperature the electrons will have some thermal energy, some electrons with enough energy to leave the valence band, cross the energy band gap E_g and enter the conduction band [8]. In the conduction band, electrons are not strongly bound to any specific atom of the lattice as they are in the valence band but are instead free to move around the semiconductor. Similarily, in the valence band the lack of an electron can be considered a quasi-particle, known as a hole, which is also free to move around the lattice.

In an intrinsic semiconductor, equal numbers of conduction band electrons and valence band holes are present, as they are created in pairs. In a process known as "doping", atoms known as "impurities" with an excess of electrons (where

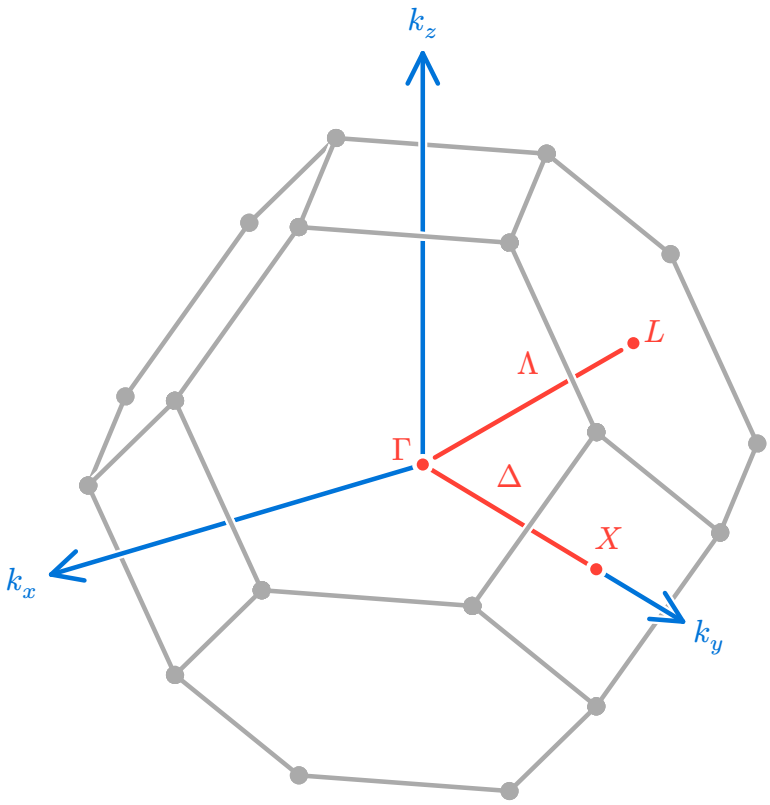

Figure 2: First Brillouin zone of the FCC grid, with the main crystallographic points and lines shown.

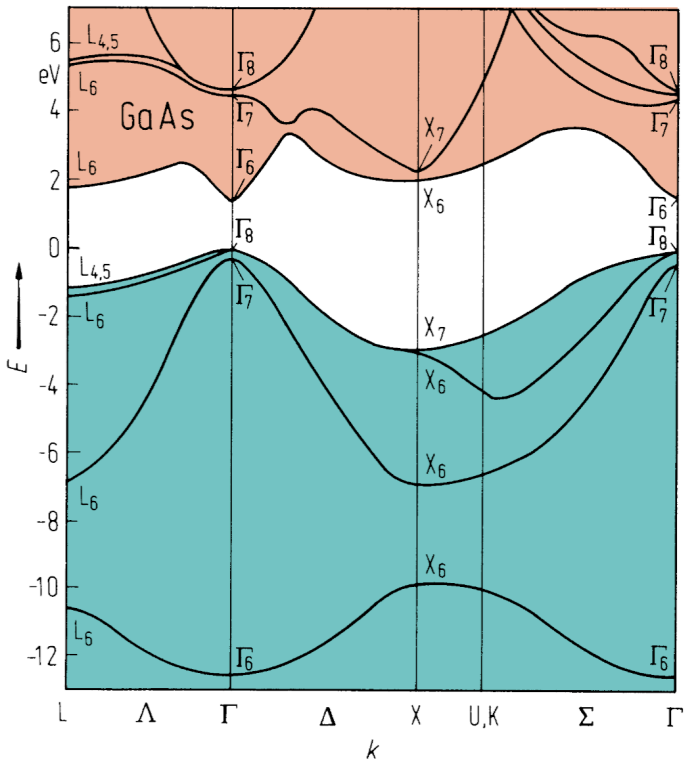

Figure 3: Band-diagram of GaAs, reprinted with changes from [13]. Valence band and below shown in blue, conduction band and above shown in beige, band gap in white.

they are known as "donors") or a lack of electrons (where they are known as "acceptors") are inserted in the lattice. If at room temperature all the impurities can be considered ionized, meaning their electron (or hole) enters the conduction band (or valence band) and the impurity is left with a positive (or negative) charge, an excess of electrons in the conduction band (or holes in the valence band) can be introduced.

For the devices considered in this work, the conduction band electrons make up the majority of the current flow [14], and as such the holes will be neglected.

In a semiconductor, electrons tend to be distributed in energy such that higher energies are exponentially less likely than lower energies [15]. As such, local minima in the band structure diagram will tend to have a higher density of electrons, while higher energy levels far from a local minima tend not to have many electrons occupying them. While simulating the full band structure diagram for the conduction band is possible [16], in this work only the wave vectors close to the local minima are considered. These local minima in energy are referred to as "valleys".

Around a valley, an often-used approximation for the energy of the electron is a first order non-parabolic band structure [17] where

$$E(k) = \frac{\hbar^2 k^2}{(1 + \alpha E(k))m^*}, \tag{3}$$

k being the magnitude of the wave vector relative to center of the valley, $E(k)$ the energy relative to the bottom of the valley and $\hbar$ being the reduced Planck constant. The parameter α is called the "non-parabolicity constant" of the valley and m^* the "effective mass", typically given in relation to the electron rest mass m_0. This energy-wave number relation is indentical to an electron in vacuum with an electron mass of $(1 + \alpha E(k))m^*$.

The group velocity of the electron $\vec{v}$ relates to the energy of the electron by [16]

$$\vec{v} = \frac{1}{\hbar}\frac{\mathrm{d}E}{\mathrm{d}\vec{k}}. \tag{4}$$

For the first order non-parabolic band structure, this evaluates to [16]

$$\vec{v} = \frac{\hbar\vec{k}}{(1 + 2\alpha E)m^*}. \tag{5}$$

While experiencing an electric field $\vec{\mathbb{E}}$, the electron accelerates, changing the wave vector (and consequently the velocity) by [16]

$$\frac{\mathrm{d}\vec{k}}{\mathrm{d}t} = -\frac{q_0}{\hbar}\vec{\mathbb{E}}. \tag{6}$$

In this work, the valleys at Γ, L and X[(1)] are modelled. The values of the properties of the valleys are presented in Table 1.

2.2. Electron scattering

Electrons in the conduction band interact by exchanging energy and momentum with the semiconductor crystal in scatter events. While not truly instantaneous, the time scales of the scatter events are short enough that in our Monte Carlo method they are considered to happen instantaneously.

Scattering mechanisms are characterized by a probability rate $\mathcal{P}_m\left(\vec{k},\vec{k'}\right)$, the average number of scatters per unit time for an electron in state $\vec{k}$ to be scattered into $\vec{k'}$, per unit $\vec{k'}$ volume. Integrating over all possible $\vec{k'}$, the probability rate $\mathcal{P}_m\left(\vec{k}\right) = \int_{V_{k'}} \mathcal{P}_m\left(\vec{k},\vec{k'}\right) \mathrm{d}\vec{k'}$ is the probability rate that an electron in state $\vec{k}$ scatters regardless of destination state $\vec{k'}$. Scattering mechanisms where $\mathcal{P}_m\left(\vec{k},\vec{k'}\right)$ is independent of $\vec{k'}$ are called "isotropic" mechanisms, and mechanisms where $\mathcal{P}_m\left(\vec{k},\vec{k'}\right) = 0$ for $E\left(\vec{k}\right) \neq E\left(\vec{k'}\right)$ (i.e., scatters may only be to states of the same energy) are called "elastic" mechanisms.

Scatters may be intravalley, where the momentum transfer between $\vec{k}$ and $\vec{k'}$ is small enough the electron stays in the same valley, or they may be intervalley, where the momentum transfer is large enough to have $\vec{k}$ and $\vec{k'}$ in different valleys. Additionally, intervalley scatters may be equivalent-intervalley where an electron scatters from one point in a valley into another equivalent point of the same valley, or non-equivalent intervalley where the electron enters a different valley.

The probability rate $\mathcal{P}_m\left(\vec{k},\vec{k'}\right)$ can be found using Fermi's golden rule [18]

$$\mathcal{P}_m\left(\vec{k},\vec{k'}\right) = \frac{2\pi}{\hbar}\langle k'|\Delta H|k\rangle D(E')\delta\left(E_{\text{system}} - E'_{\text{system}}\right) \tag{7}$$

where ΔH is the pertubation to the system's Hamiltonian introduced by the specific scattering mechanism, $D(E)$ is the electron density of states at energy E and $\delta\left(E_{\text{system}} - E'_{\text{system}}\right)$ expresses the total conservation of energy before and after the scatter, $\delta(\cdot)$ being Dirac's delta-function.

In this work, phonon scattering and impurity scattering are the mechanisms taken into account. Phonon scattering can be further divided into many different subcategories, as will be described in Section 2.2.1. Impurity scattering is described in Section 2.2.2. All parameters of interest for scattering are listed in Table 1.

(1) The local minima is not quite at the X-point of the reciprocal lattice, but about 10% closer to the Γ-point [13]. Despite this, the valley will be referred to as the X-valley.

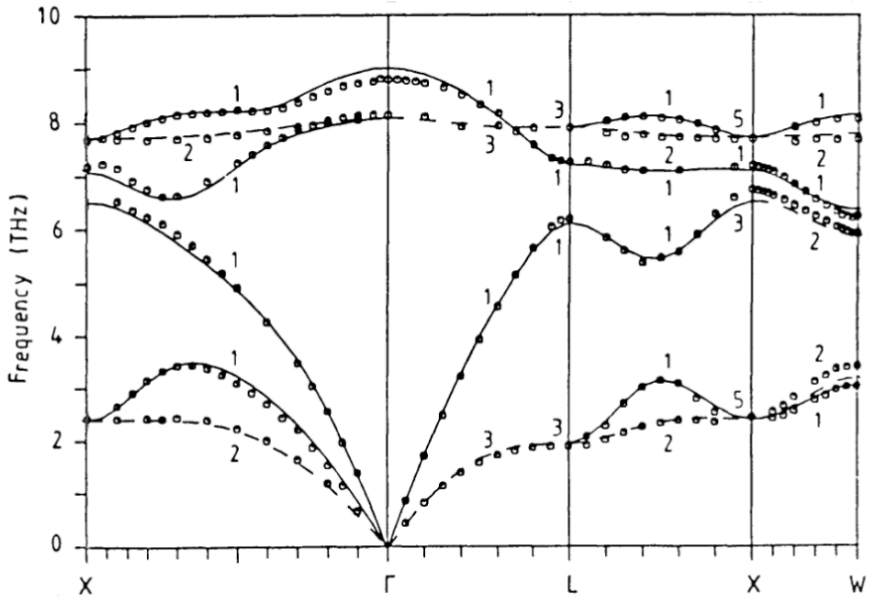

Figure 4: Phonon spectrum diagram for GaAs, reprinted with changes from [18]

2.2.1. Phonon scattering

The thermal energy of the lattice is discretized into vibrations of the atoms in the semiconductor lattice. These discretized vibrations are known as "phonons", with energies E (related to their frequency ω^p) and a momentum (related to their wave vector $\vec{k}$). The phonons also form a band structure relating the wave-vector and energy of the phonons, illustrated in Figure 4.

Close to the center (Γ) of the Brillouin zone, there are two branches of frequency for a phonon, as shown in Figure 4. The phonon can either have a long wavelength where the frequency approaches zero as the wave vector approaches the Γ point of the reciprocal lattice, in which case the phonon is referred to as an "acoustic" phonon, or the frequency can approach a finite value at Γ in which case the phonon is referred to as an "optical" phonon.

2.2.1.1. Acoustic phonons

Acoustic phonons only exist close to the Γ-point, meaning they have low momentum. Conservation of momentum implies an electron absorbing or emitting an acoustic phonon will remain in the same valley, meaning this scattering mechanism is only intravalley.

The energy of the acoustic phonon is typically considered very small in comparison to the energy of an electron. Therefore, the energy of the electron after having absorbed or emitted an acoustic phonon can be considered the same as before the scatter, meaning the scatter is elastic. For acoustic phonons, the probability rate is given as [10]

$$\mathcal{P}\left(\vec{k},\vec{k'}\right) = \frac{2\pi k_B T D_a^2}{\hbar \rho s^2 V_{k'}} G\left(\vec{k},\vec{k'}\right)\delta(E(k') - E(k))$$
$$\sqrt{G\left(\vec{k},\vec{k'}\right)} = \sqrt{\frac{1+\alpha E(k)}{1+2\alpha E(k)}}\sqrt{\frac{1+\alpha E(k')}{1+2\alpha E(k')}} + \tag{8}$$
$$+\sqrt{\frac{\alpha E(k)}{1+2\alpha E(k)}}\sqrt{\frac{\alpha E(k')}{1+2\alpha E(k')}}\cos\frac{\vec{k}\cdot\vec{k'}}{kk'}$$

where

- T is the temperature of the lattice
- k_B is Boltzmann's constant
- $\hbar$ is the reduced Planck's constant
- $V_{k'}$ is the volume of the Brillouin zone in $\vec{k}'$-space
- ρ is the density of the host semiconductor
- s is the speed of sound in the host semiconductor
- D_a is the acoustic deformation potential

Due to the dependance on the direction of k' in the $G\left(\vec{k},\vec{k'}\right)$ term, this mechanism is not isotropic.

Integrating among all destination states $\vec{k'}$ we find

$$\mathcal{P}\left(\vec{k}\right) = \frac{(2m^*)^{\frac{3}{2}} k_B T D_a^2}{2\pi\rho s^2\hbar^4}\frac{(1+\alpha E)E\left[(1+\alpha E(k))^2 + \frac{1}{3}(\alpha E(k))^2\right]}{1+2\alpha E(k)} \tag{9}$$

2.2.1.2. Intravalley optical phonons

For an optical phonon to result in intravalley scattering, conservation of momentum implies the wave vector of the phonon must be close to the Γ-point. As optical phonons have significant energy, we must distinguis between absorbing and emitting scatters. [10] derives

$$\mathcal{P}\left(\vec{k},\vec{k'}\right) = \frac{4\pi^2 q_0^2 \omega^p}{V_{k'}\ |\vec{k}-\vec{k'}|^2}\left(\frac{1}{\varepsilon_\infty} - \frac{1}{\varepsilon_0}\right)G\left(\vec{k},\vec{k'}\right)\cdot$$
$$\cdot\begin{cases} N^p\delta(E(k') - E(k) - \hbar\omega^p) & \text{absorption} \\ (N^p+1)\delta(E(k') - E(k) + \hbar\omega^p) & \text{emission}\end{cases} \tag{10}$$
$$N^p = \frac{1}{\exp\left(\frac{\hbar\omega^p}{k_B T}\right) - 1}$$

where

- q_0 is the fundamental (electron) charge
- ω^p is the frequency of the optical phonon

- ε_0 and ε_∞ the low- and high-frequency dielectric constant of the host semiconductor

Again we see a dependance on k' both in the term $G\left(\vec{k},\vec{k'}\right)$ and also in the $\left|\vec{k}-\vec{k'}\right|^2$ term in the denominator, meaning this mechanism is not isotropic.

Integrating among all destination states $\vec{k'}$ we find

$$\begin{aligned}
\mathcal{P}\left(\vec{k}\right) &= \frac{q_0\sqrt{m^*}\omega_p}{\sqrt{2}\hbar}\left(\frac{1}{\varepsilon_\infty}-\frac{1}{\varepsilon_0}\right)\frac{1+2\alpha E'}{\sqrt{(1+\alpha E)E}}F_0(E(k),E'(k))\cdot \\
&\quad\cdot\begin{cases}N^p & \text{absorption}\\ (N^p+1) & \text{emission}\end{cases} \\
E'(k) &= \begin{cases}E(k)+\hbar\omega^p & \text{absorption}\\ E(k)-\hbar\omega^p & \text{emission}\end{cases} \\
F_0(E,E') &= C^{-1}\left(A\ln\left|\frac{\sqrt{(1+\alpha E)E}+\sqrt{(1+\alpha E')E'}}{\sqrt{(1+\alpha E)E}-\sqrt{(1+\alpha E')E'}}\right|+B\right) \\
A &= \left(2(1+\alpha E)(1+\alpha E')+\alpha((1+\alpha E)E+(1+\alpha E')E')\right)^2 \\
B &= -2\alpha\sqrt{(1+\alpha E)E(1+\alpha E')E'}\cdot \\
&\quad\cdot\left[4(1+\alpha E)(1+\alpha E')+\alpha((1+\alpha E)E+(1+\alpha E')E')\right] \\
C &= 4(1+\alpha E)(1+\alpha E')(1+2\alpha E)(1+2\alpha E').
\end{aligned} \tag{11}$$

2.2.1.3. Intervalley optical phonons

For scattering between two valleys i (source) and j (destination), where the phonon wave vector is close to $\vec{k}_i-\vec{k}_j$, [10] derives

$$\begin{aligned}
\mathcal{P}\left(\vec{k},\vec{k'}\right) &= \frac{\pi Z_j D_{i,j}^2}{\rho\omega_{i,j}^p V_{k'}}G_{i,j}(E(k),E'(k'))\cdot \\
&\quad\cdot\begin{cases}N_{i,j}^p\delta\left(E'(k')-E(k)+\Delta E_{i,j}-\hbar\omega_{i,j}^p\right) & \text{absorption}\\ \left(N_{i,j}^p+1\right)\delta\left(E'(k')-E(k)+\Delta E_{i,j}+\hbar\omega_{i,j}^p\right) & \text{emission}\end{cases} \\
G_{i,j}(E,E') &= \frac{(1+\alpha_i E)\left(1+\alpha_j E'\right)}{(1+2\alpha_i E)\left(1+2\alpha_j E'\right)} \\
N_{i,j}^p &= \frac{1}{\exp\left(\frac{\hbar\omega_{i,j}^p}{k_B T}\right)-1}
\end{aligned} \tag{12}$$

where

- $\omega_{i,j}^p$ is the phonon frequency for the intervalley phonon

- Z_j is the number of equivalent valleys for the destination valley (discounting the source valley if they are of the same type)
- $D_{i,j}$ the intervalley deformation potential
- $\Delta E_{i,j}$ the difference in energy minima for the source and destination valley

We see probability is independent on the direction of $\vec{k'}$, meaning this mechanism is isotropic.

Integrating among all destination states $\vec{k'}$ we find

$$\begin{aligned}\mathcal{P}\left(\vec{k}\right) &= \frac{Z_j\left(m_j^*\right)^{\frac{3}{2}} D_{i,j}^2}{\sqrt{2}\pi\rho\omega_{i,j}^p\hbar^3}\sqrt{\left(1+\alpha_j E'\right)E'}\left(1+2\alpha_j E'\right)G_{i,j}(E,E')\cdot \\ &\cdot\begin{cases} N_{i,j}^p & \text{absorption} \\ \left(N_{i,j}^p+1\right) & \text{emission}\end{cases} \\ E' &= \begin{cases} E+\Delta E_{i,j}+\hbar\omega_{i,j}^p & \text{absorption} \\ E+\Delta E_{i,j}-\hbar\omega_{i,j}^p & \text{emission}\end{cases}\end{aligned} \tag{13}$$

2.2.2. Ionized impurities

For impurity scattering, the Conwell and Weisskopf (CW) approach from [11] is used. This scattering mechanism is isotropic,

$$\begin{aligned}\mathcal{P}\left(\vec{k}\right) &= \frac{\sqrt{2}\pi n_i Z^2 b^2}{\sqrt{m^* q_0^2}}\frac{(1+2\alpha E)E^2}{((1+\alpha E)E)^{\frac{3}{2}}} \\ b &= \left(\frac{3}{4\pi n_i}\right)^{\frac{1}{3}}\end{aligned} \tag{14}$$

where

- Z is the average charge per impurity
- n_i is the density of impurities

2.3. The Schottky barrier diode

The rectifying metal-semiconductor contact was first implemented by Braun in 1874 as a point contact between a “cat’s whisker” sharpened metal wire and an exposed semiconductor surface. In 1898, this device was successfully used as a high-sensitivity radio detector and in the years following became the primary type of detector in radio devices. In the following decades the device found use in many fields, such as microwave radar systems and laboratory devices for power measurement. In 1942, Bethe developed the thermionic emission theory [19], which will be outlined in this section. Due to the poor quality and purity of semiconductor crystals at the time and the unpredictability of the point contact,

the theoretical behaviour of the device was difficult to verify. In the 1960′s, the planar Schottky barrier diode was introduced, fabricated by evaporating metals onto high quality semiconductor crystals in a cleanroom environment, showing close to the ideal behaviour predicted by the thermionic emission theory [20].

The Schottky barrier diode is a semiconductor device consisting two metal-semiconductor junctions. The first junction is a metal to low-concentration n -doped semiconductor (called the "active region"), forming a Schottky contact. The second junction is with a heavily n-doped semiconductor (called the "buffer region") forming an "ohmic contact". The Schottky contact is a rectifying element, having an exponential current-voltage curve allowing a large positive current when the device has a positive voltage applied, but only allowing a very small negative current at reverse voltage. The ohmic does not affect the current-voltage characteristics of the device (other than a series resistance) but allows electrons to leave the semiconductor and enter the metal cathode.

Similar to a semiconductor, a metal can also consist of a crystal structure, giving rise to energy bands electrons can reside in. Unlike a semiconductor, a metal does not have a band gap between the conduction and valence band, instead the two bands intersect, meaning the metal has electrons in the conduction band even at zero temperature. The mean electron energy (discounting the density of states), called the Fermi energy E_F [15] intersects the conduction band, meaning the metal will have a high density of free carriers and many empty electron states in the conduction band above the Fermi level.

The barrier height φ_b of the metal-semiconductor junction is the difference in energy between the Fermi level of the metal and the conduction band energy of the semiconductor. For an ideal Schottky contact, this work function can be predicted as $\varphi_b = \chi - W_M$, where W_M is the "work function" of the metal, the energy difference between Fermi level and vacuum energy of the system, χ is the "electron affinity" of the semiconductor, the energy difference between the conduction band and vacuum energy. In practice, imperfections such as surface oxides in the junctions mean the true barrier height φ_b is poorly predicted by this energy difference $W_M - \chi$. Instead the barrier height and has to be extracted from experiments [14], [21].

2.3.1. The Schottky contact

If the barrier height is positive, meaning the work function of the metal is lower than the conduction band energy of the semiconductor, a Schottky contact is formed.

Since $W_M > \chi$ the Fermi energy of the electrons in the metal is lower than the minimum energy of the electrons in the conduction band of the semiconductor.

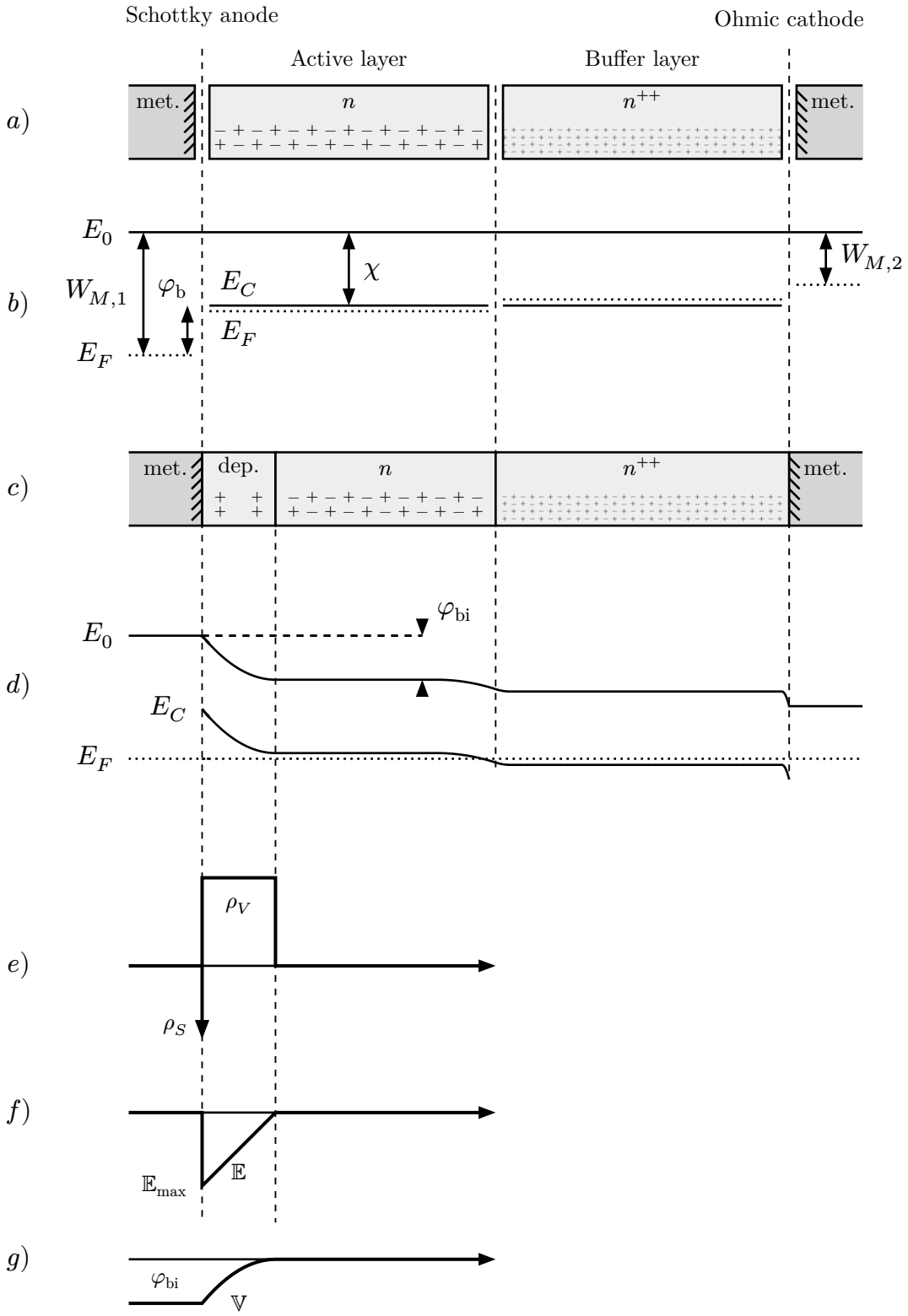

Figure 5: Diagram of a Schottky barrier diode showing
a) System before contact, consisting of the anode, active and buffer region, and cathode,
b) Band diagram before contact, E_C the lowest energy level of the conduction band,
c) Schottky barrier diode in contact, with a depletion region having been formed,
d) Band diagram of diode in contact,
e) Charge distribution, *f*) Electric field, *g*) Voltage

Above the Fermi energy the number of empty states for electrons to occupy grows rapidly, therefore the electrons from the semiconductor are free to flow into the empty conduction band states in the metal. On the contrary, electrons from the metal have low energy compared to the empty states in the semiconductor, therefore the electrons in the metal will very rarely flow from metal to semiconductor. As contact is made between metal and semiconductor electrons will predominantly flow from semiconductor to metal. As the region of the semiconductor next to the metal is depleted of electrons, the surface charge in the metal give rise to an electric field opposing the flow of electrons. Equilibrium is reached when the flow of electrons into the metal is fully counteracted by this electric field, as illustrated in Figure 5 *c* and *d*).

As a first approximation, one can postulate that the semiconductor closest to the metal is fully depleted of electrons and that the active region next to this region being fully neutral, as illustrated in Figure 5 c). Let the doping concentration of the semiconductor be N_D, thus the depletion region will have a volume charge density $\rho_V = q_0 N_D$, as shown in Figure 5 *f*). Let the depletion region have an extent of x_d. Due to local conservation of charge, the surface charge on the metal will be $\rho_S = -x_d \rho_V$

$$\begin{aligned} \mathbb{E}_x(x) &= \frac{1}{\varepsilon_0 \varepsilon_r}\left(\rho_S + \int_{0^+}^{x} \rho_V \,\mathrm{d}x\right) = \frac{(x_d - x) q_0 N_D}{\varepsilon_0 \varepsilon_r} \\ \mathbb{V}(x) &= -\int_0^x \mathbb{E}_x \,\mathrm{d}x = -\frac{(x_d - x)^2 q_0 N_D}{2\varepsilon_0 \varepsilon_r} \\ \varphi_{\mathrm{bi}} - \mathbb{V}_{\mathrm{ext}} &= \mathbb{V}(x_d) - \mathbb{V}(0) = \frac{x_d^2 q_0 N_D}{2\varepsilon_0 \varepsilon_r} \end{aligned} \tag{15}$$

$\mathbb{V}_{\mathrm{ext}}$ is the externally applied voltage between the anode and cathode and ε_r is the low-frequency relative dielectric permittivity of the semiconductor. For GaAs, ε_r is given in Table 1.

The the potential over the diode at thermal equilibrium, known as the built-in potential φ_{bi}, can also be statistically estimated from thermodynamic theory as [15]:

$$\begin{aligned} \varphi_{\mathrm{bi}} &= \frac{1}{q_0}(W_M - \chi) - \varphi_n \\ \varphi_n &= \frac{k_B T}{q_0} \ln\left(\frac{N_D}{N_c}\right), \end{aligned} \tag{16}$$

where N_c is the effective density of states of the conduction band of the semiconductor.

The "thermionic emission" theory for Schottky junctions assumes that the main current contribution is electrons flowing from the semiconductor to the metal, and electrons close to the junction (within the mean free path length) follow a Maxwell-Boltzmann distribution. One can derive that for a Schottky junction with an applied bias $\mathbb{V}_{\text{exp}}$, the current density from semiconductor to metal is [14]

$$J_{\text{s.c.} \to \text{ met}} = A^* T^2 \exp \frac{-q_0 \varphi_{\text{b}}}{k_B T} \exp \frac{q_0 \mathbb{V}_{\text{ext}}}{k_B T} \tag{17}$$

where A^* is the "Richardsson constant" for the semiconductor material. To find the opposite current going from the metal to semiconductor, as a first order approximation the barrier height φ_b can be considered constant regardless of the applied voltage. Therefore the current going from metal to semiconductor can be assumed independent from the applied voltage. Imposing the condition that the total current $J_{\text{s.c.} \to \text{ met.}} - J_{\text{met.} \to \text{ s.c.}}$ is zero when no external bias is applied, then

$$J_{\text{met.} \to \text{ s.c.}} = A^* T^2 \exp \frac{-q_0 \varphi_{\text{b}}}{k_B T}. \tag{18}$$

The total current over the diode with area A is thus

$$\begin{aligned} I &= A(J_{\text{s.c.} \to \text{ met.}} - J_{\text{met.} \to \text{ s.c.}}) = \\ &= A A^* T^2 \exp \frac{-q_0 \varphi_{\text{b}}}{k_B T} \left(\exp \frac{q_0 \mathbb{V}_{\text{ext}}}{k_B T} - 1 \right) = \\ &= I_0 \left(\exp \frac{q_0 \mathbb{V}_{\text{ext}}}{k_B T} - 1 \right) \end{aligned} \tag{19}$$

where I_0 is called the (reverse) "saturation current" of the diode.

2.4. The ohmic contact

If instead the barrier height φ_b is negative, meaning the work function of the metal is higher than the semiconductor, an ohmic contact is formed. Instead of a depletion region, an accumulation region is formed, which does not create the rectifying behaviour of the Schottky contact. In practice however, such a metal-semiconductor pair can be hard to find. A widely used alternative is to rely on field emissions over the junction, where very high doping levels result in a depletion region small enough that electrons may quantum tunnel over it [14], [15], [22]. This technique is widely used, and may be enhanced by various treatment methods such as heating the contact to let the metal melt into the semiconductor and form an alloy [14].

An ohmic contact is classified by its contact resistance, where an ideal ohmic contact has zero resistance and thus no drop in voltage over it. Common for

Monte Carlo simulations is to model an ohmic contact as a boundary which is kept in local thermal equilibrium [8].

2.5. Non-ideal effects in the Schottky barrier diode

Various effects can cause a diode to have a current-voltage relationship that varies from the one presented above. One such effect can be due to oxides being present at the metal-semiconductor interface. The voltage drop over the oxide is proportional to the maximum electric field in the structure, which is in turn proportional to the applied voltage, thus the effective barrier height $\varphi_{\mathrm{b,eff}}$ can be assumed to linearly depend on the applied voltage: $\varphi_{\mathrm{b,eff}} = \varphi_{\mathrm{b},0} + \beta \mathbb{V}_{\mathrm{ext}}$, with β the linearity constant [14]. Substituting into eq. 19, we get

$$\begin{aligned} I &= AA^*T^2 \exp \frac{-q_0\left(\varphi_{\mathrm{b},0} + \beta \mathbb{V}_{\mathrm{ext}}\right)}{k_B T}\left(\exp \frac{q_0 \mathbb{V}_{\mathrm{ext}}}{k_B T} - 1\right) = \\ &= I_{\mathrm{eff},0} \exp \frac{q_0 \mathbb{V}_{\mathrm{ext}}}{n k_B T}\left(1 - \exp \frac{-q_0 \mathbb{V}_{\mathrm{ext}}}{k_B T}\right) \end{aligned} \tag{20}$$

for the ideality factor $n = \frac{1}{1-\beta}$. For V sufficiently larger than $\frac{k_B T}{q_0}$, the above can be simplified into a form similar to eq. 19:

$$I = I_{\mathrm{eff},0}\left(\exp \frac{q_0 \mathbb{V}_{\mathrm{ext}}}{n k_B T} - 1\right) \tag{21}$$

Both the active layer, buffer layer and ohmic contact may provide some series resistance in the device. When an external voltage $\mathbb{V}_{\mathrm{ext}}$ is applied over the whole device, the effective voltage over the Schottky junction is lowered by $R_s I$ where R_s is the effective series resistance of all the elements in the diode. Included this in the diode equation gives:

$$I = I_{\mathrm{eff},0}\left(\exp \frac{q_0(\mathbb{V}_{\mathrm{ext}} - R_s I)}{n k_B T} - 1\right). \tag{22}$$

2.6. Methods of simulation for semiconductor devices

Accurately predicting the performance of a Schottky barrier diode requires simulating the devices to extract the current-voltage relation and parasitic capacitance, and to model the noise of the device. Noise in a Schottky barrier diode-based mixer is higher than other mixer technologies such as SIS- or HEB-mixers and is typically the limiting component in a receiver chain and as such accurate modeling is important [5]. At low fields inside the active region of the Schottky barrier diode, the noise of the device is accurately described by considering only Johnson and shot noise as the sources of noise in the device; however at higher fields strengths considering only these noise sources under-

predicts the noise of the device. At high fields and high current densities, the effects of electron heating and intervalley scattering become important sources of noise [7].

The most accurate approach for semiconductor simulation is a quantum approach where the wave functions of the carriers is solved with respect to the Schrödinger equation. Even with a number of approximations applied, this method is very difficult to apply for device simulation [23]. Typically the semiclassical Boltzmann transport equation coupled to Poisson's equation is instead used as the basis for simulating charge transport in semiconductors.

2.6.1. Solving the Boltzmann transport equation

The Boltzmann transport equation is derived by applying Liouville's theorem, which asserts that the time-variant carrier distribution function $f\left(\vec{r}, \vec{k}, t\right)$ has zero time-derivative over a particle trajectory $\vec{r}(t)$ [24]:

$$\frac{\partial f}{\partial t} + \frac{\mathrm{d}r(t)}{\mathrm{d}t}\nabla_{\vec{r}} f + \frac{\mathrm{d}k(t)}{\mathrm{d}t} \cdot \nabla_{\vec{k}} f = 0 \tag{23}$$

$\frac{\mathrm{d}r(t)}{\mathrm{d}t}$ is, as previously defined, the velocity of the particle. The term $\frac{\mathrm{d}k(t)}{\mathrm{d}t} \cdot \nabla_{\vec{k}} f$ is related to the forces applied to the particle, which are composed of an external force F_{ext} from the electric field and an internal force relating to the scattering processes the particle experiences. It can thus be related to the local electric field E and the probabilities of all the scattering mechanisms being considered.

This seven-dimensional intregro-differential equation is quite challenging to solve. A number of numerical techniques can be applied to solve the equation directly, and more exotic numeric techniques like cellular automata and evolutionary algorithms can be applied.

A common simulation approach is to obtain an approximate transport model using the different moments of the equation. In the drift-diffusion method, the moments of particle concentration and momentum are used. The Boltzmann transport equation then expresses the continuity of carriers and holes, relating them to the current densities and generation-recombination rates. Typically, to obtain closed expressions for the current densities the current is assumed to be composed of a drift current being proportional to the electric field and a diffusion component proportional to the gradient of the carrier concentration. As such, information about thermal effects, velocity overshoot and other important aspects relevant to modelling the IV- and noise-characteristics of the diodes is lost. More advanced and improved drift-diffusion methods exist: one can use models for drift-currents over field strength as predicted by more advanced simulation tools such as the Monte Carlo method to model velocity overshoot, as demonstrated for Schottky barrier diodes in [25]. Additionally, one can couple

the drift-diffusion method to equations of heat transfer to model the effect of hot electrons [26].

By including a third moment of energy conservation from the Boltzmann transport equation, the hydrodynamic method is derived. No assumptions about contributions of current need to be made, and from the conservation of energy, electron heating is modelled directly. Typically, the scattering term is modelled using a relaxation time, as modelling the scattering rates directly can be impractical [23]. As such, the hydrodynamic approach can capture the effects of carrier heating into account, as demonstrated for Schottky barrier diodes in [6].

2.6.2. The Monte Carlo method

The Monte Carlo method as applied to semiconductor transport is a statistical method for sampling particle trajectories for the Boltzmann transport equation, making no a-priori assumptions about the distribution function. These trajectories are sampled by generating random numbers to select between the scattering mechanisms. As the number of samples grows large, the statistical average of the behaviour of the particle becomes equivalent to solving the Boltzmann transport equation [23]. The statistical sampling approach allows one to model the scattering mechanisms as full probability distributions over particle states, a more accurate approach than assuming all scattering mechanisms to be isotropic as one does with the relaxation time approximation. As such, the Monte Carlo method has the ability to provide the most accurate approach to solving the Boltzmann transport equation, only being limited by the model for the band structure of the semiconductor used and how the scattering mechanisms are modelled [23].

Additionally, as the Monte Carlo method is a stochastic method, the noise of the device being simulated will naturally occur in the simulation. As opposed to the numerical solutions to the Boltzmann transport equation, where noise has to be indirectly computed based on the properties predicted by the simulations, in the Monte Carlo method the noise spectra is directly provided by observing the statistical variance of the predicted currents.

3. Method

The Monte Carlo method simulates bulk semiconductors or semiconductor devices by individually tracking each carrier in the system. The carriers alternate between experiencing "free flight", where they move through the semiconductor, and scatter events where they exchange momentum and energy with the lattice. The details of free flight and scatter events are described in detail in Section 3.1.

The simulator implemented in this work can either be configured as a single- or multi-particle simulator. In the former, one particle is simulated in isolation inside a sample of bulk semiconductor and the particle is said to represent the system as a whole. This mode of simulation can compute a number of homogeneous static transport properties of the semiconductor material. In the latter, many electrons are simulated in a potentially complicated device structure. The electric field is not constant as the charge of the electrons perturb the electric field and the electrons interact with each other through the Coloumb force. The device structure is represented as a discretized grid where each cell represents the local properties of the device at that location. This allows us to simulate the intricate behaviour of any device that can be described in terms of geometry, doping and boundary conditions that the simulator supports.

A number of approximations are made in this thesis for simulating high-frequency Schottky barrier diodes. The space is assumed to be one-dimensional, where the device structure only extends in the x-direction, and the fields are assumed to point only longitudunally along this direction. Furthermore, the devices intended to be simulated in this work are electrically small, with physically dimensions being much smaller than the wavelengths of the frequencies they operate at. As such, a quasi-static approximation is used, where the magnetic field is assumed to be zero and Faraday's law of induction can be ignored. Lastly, as n-type Schottky barrier diodes are majority carrier devices, with electrons carry the majority of the current flowing through the device, holes are disregarded and only electrons are simulated.

Valley:		Γ	*L*	*X*
Lattice constant a [nm]		0.563		
Density ρ [kg/m^3]		5370		
Speed of sound s [m/s]		5220		
Low-frequency dielectric constant ε_0 [F/m]		12.53		
High-frequency dielectric constant ε_∞ [F/m]		10.82		
Electron affinity χ [eV]		4.07		
Effective density of states N_c [cm^{-3}]		4.21×10^{17}		
Richardsson constant A^* [A / K^2 cm^2]		0.494		
Effective mass [m_0]		0.067	0.35	0.85
Minimum energy [eV]		1.42	1.729	1.906
Nonparabolicity α [eV^{-1}]		0.61	0.222	0.061
Acoustic deformation potential D_a [eV]		7.0		
Optical phonon energy $\hbar\omega^p$ [meV]		36.1	36.1	36.1
Intervalley deformation potential $D_{i,j}$ [eV/m]		$1 \cdot 10^{11}$		
Charge per impurity Z [q_0]		+1		
Intervalley phonon energy $\hbar\omega^p_{i,j}$ [meV]	Γ	–	27.8	29.3
	L	27.8	–	29.3
	X	29.3	29.3	–

Table 1: Parameters used for GaAs in this work

3.1. Electron motion

When simulating a carrier, a semi-classical approach is used, where the carrier strictly alternates between free flight where it accelerates from the local electric field and moves through the semiconductor lattice, and interacting with the lattice in scatter events. During free flight, the carrier is considered a classical particle with a known position $\vec{r}$ and a known velocity $\vec{v} = \frac{\mathrm{d}\vec{r}}{\mathrm{d}t}$, while during the instantaneous scatter events the carrier is considered a quantum wave.

The free flights accelerate the carrier due to the force applied by the electric field, and move the carrier based on its velocity. After a free flight of duration Δt, short enough that the electric field $\vec{\mathbb{E}}$ and electron energy E can be considered constant through the flight, the resulting position of the electron after the flight can be found by integrating eqs. 5 and 6,

$$
\begin{aligned}
\vec{k}(t=\Delta t)-\vec{k}(t=0) &= -\Delta t\frac{q_0}{\hbar}\vec{\mathbb{E}} \\
\vec{r}(t=\Delta t)-\vec{r}(t=0) &= \int_0^{\Delta t}\vec{v}(t)\,\mathrm{d}t = \int_0^{\Delta t}\frac{\hbar\vec{k}(t)}{(1+2\alpha E)m^*}\,\mathrm{d}t \\
&= \frac{1}{(1+2\alpha E)m^*}\int_0^{\Delta t}\hbar\left[\vec{k}(t=0)-t\frac{q_0}{\hbar}\vec{\mathbb{E}}\right]\mathrm{d}t \\
&= \frac{1}{(1+2\alpha E)m^*}\left(\Delta t\hbar\vec{k}(t=0)-\frac{\Delta t^2}{2}q_0\vec{\mathbb{E}}\right).
\end{aligned}
\tag{24}
$$

The time Δt is related to the probabilities $\mathcal{P}_m$ of of each scatter event to happen per unit time. Let $t=0$ be the time the free flight started. The probability of the electron not having scattered at time t is [11]

$$
\mathbb{P}_{\text{no scatter before}}(t) = \exp\left(-\int_0^t \mathcal{P}\left(\vec{k}(t)\right)\mathrm{d}t\right) \tag{25}
$$

where $\mathcal{P}\left(\vec{k}\right)$ is the sum of each individiual scattering probability rates $\sum_m \mathcal{P}_m\left(\vec{k}\right)$ from the scattering mechanisms defined in Section 2.2. Thus the probability rate of suffering a scatter in the time interval $[t, t+\mathrm{d}t]$ is

$$
\begin{aligned}
\mathcal{P}_{\text{scatter}}(t)\,\mathrm{d}t &= \mathbb{P}_{\text{no scatter before}}(t)\mathcal{P}\left(\vec{k}(t)\right)\mathrm{d}t \\
&= \mathcal{P}\left(\vec{k}(t)\right)\exp\left(-\int_0^t \mathcal{P}\left(\vec{k}(t)\right)\mathrm{d}t\right)\mathrm{d}t
\end{aligned}
\tag{26}
$$

The difficulty in evaluating this probability rate is evaluating the integral as $\vec{k}(t)$ changes throughout the flight. To remedy this difficulty, a ficticious scattering mechanism called a "self scatter" is introduced to the system. This mechanism, first introduced in [9], is defined to have the electrons state after the scatter be the same as before scatter, $\vec{k'}=\vec{k}$. This means that introducing this ficticious mechanism will not change the physical behaviour of the system. The probability rate of this mechanism is defined to be

$$
\mathcal{P}_{\text{self-scatter}} \doteq \mathcal{P}_{\max} - \sum_m \mathcal{P}_m\left(\vec{k}\right) \tag{27}
$$

with $\mathcal{P}_{\max}$ a constant chosen to be larger than the sum of all other scattering probabilities for all wave vectors $\vec{k}$ that may occur in the simulation. With this mechanism introduced, the total probability rate is a constant $\mathcal{P}_{\text{scatter}} = \mathcal{P}_{\max}$. The probability of suffering a scatter in the time interval is thus:

$$
\mathcal{P}_{\text{scatter}}(t)\,\mathrm{d}t = \mathcal{P}_{\max}\exp(-t\mathcal{P}_{\max})\,\mathrm{d}t, \tag{28}
$$

an exponential distribution with rate $\mathcal{P}_{\max}$. To sample such a distribution, uniformly sample a number r between zero and one and let

$$t_{\text{scatter}} = \frac{1}{\mathcal{P}_{\max}} \ln(r). \tag{29}$$

Once t_{scatter} has been sampled, the specific mechanism is sampled. Each mechanism's probability $\mathcal{P}_m\left(\vec{k}(t_{\text{scatter}})\right)$ (including the self-scatter) is evaluated and a random number is generated to select the specific mechanism. Once the mechanism has been selected, $\vec{k}'$ is sampled from the distribution $\mathcal{P}_m\left(\vec{k}(t_{\text{scatter}}), \vec{k}'\right)$. This is trivial for isotropic mechanisms (as $\vec{k}'$ is uniformly distributed), but for non-isotropic mechanisms more care is needed.

3.2. Single Particle Monte Carlo

In the single-particle simulation, one single carrier is simulated, from which a number of transport propeties can be predicted. As the simulation runs for a long time, by ergodicity the carrier can be assumed to visit a large enough part of the phase space to be able to represent the system as a whole. Some transport properties can be formulated as the statistical average of some quantity for many particles in a semiconductor. These properties can be computed from the simulation by taking the mean of the quantity of the carrier over the simulation time.

Some transport properties may be formulated as the statistical standard deviation of some quantity for many particles. For example, as will be further described in Section 3.2.1, the diffusion coefficient D is related to the standard deviation of the particle position $\vec{r}$, an as such can not be predicted by only simulating one single particle. To compute such properties, the single-particle method may easily be extented into the "ensemble" single-particle Monte Carlo method. Here, the single-particle method is ran many times, simulating many particles in isolation not interacting with each other. This method may also be used for the aforementioned statistical average transport properties to reduce the simulation time as many simulations can be ran in parallel on the same machine.

In the single-particle Monte Carlo method, the electric field must be constant throughout the simulation domain. While the carrier does have a physical charge which will introduce a pertubation to the electric field, this pertubation excerts no force on the particle itself, and can as such be ignored.

In Figure 6 and 7, an example electron's path is traced in two of the three spatial dimensions as it travels through a bulk sample of intrinsic GaAs. The electron starts at the origin of the coordinate system. Red crosses indicate scattering events and regularly spaced dots indicate the free flight path. The dots are placed

every 20 fs. Black, orange and purple dots show the electron in the Γ-, L- and X -valley respectively.

3.2.1. Simulations performed

The transport properties simulated in this work are the "mobility" μ and "diffusion coefficient" D at different field strengths. For these, single-particle and ensemble single-particle Monte Carlo are used. In both cases, the carrier(s) are simulated for 100 ps and to avoid transient effects at the start of the simulation the first 10 ps are discarded. The impurity density for impurity scattering is set to $10^{15}\mathrm{cm}^{-3}$.

Mobility describes the relation between mean velocity of electrons in the semiconductor to the applied field,

$$v(\mathbb{E}) = \mu(\mathbb{E})\mathbb{E}. \tag{30}$$

As such, the mobility can be simulated using single-particle Monte Carlo, with the mean velocity being recorded for the particle being simulated.

GaAs, like all semiconductors, shows the phenomenon of "velocity saturation", where at low fields the mobility is constant over $\mathbb{E}$, but as the electric field becomes sufficiently strong the velocity saturates to a constant value. Like all $III-V$-semiconductors, negative differential mobility is also present, where above a critical field $\mathbb{E}_{\text{crit}}$ the velocity decreases with further increased field. The results from the simulator are compared against measured data from [27] and a model described in [28].

The diffusion coefficient D relates the diffusion current to the gradient of carrier concentration over space,

$$J_{\text{diff}} = q_0 D \frac{\mathrm{d}n}{\mathrm{d}x} \tag{31}$$

The diffusion coefficient can be estimated using the ensemble single-particle Monte Carlo, by relating it to the standard deviation of the position of many simulated carriers: [11]

$$D = \frac{1}{2}\frac{\left\langle (x - \langle x \rangle)^2 \right\rangle}{t}. \tag{32}$$

The diffusion coefficient is compared to a previous Monte Carlo study in [29]. At low field strength, the Einstein relation is expected to hold: [15]

$$D = \frac{k_B T}{q_0}\mu. \tag{33}$$

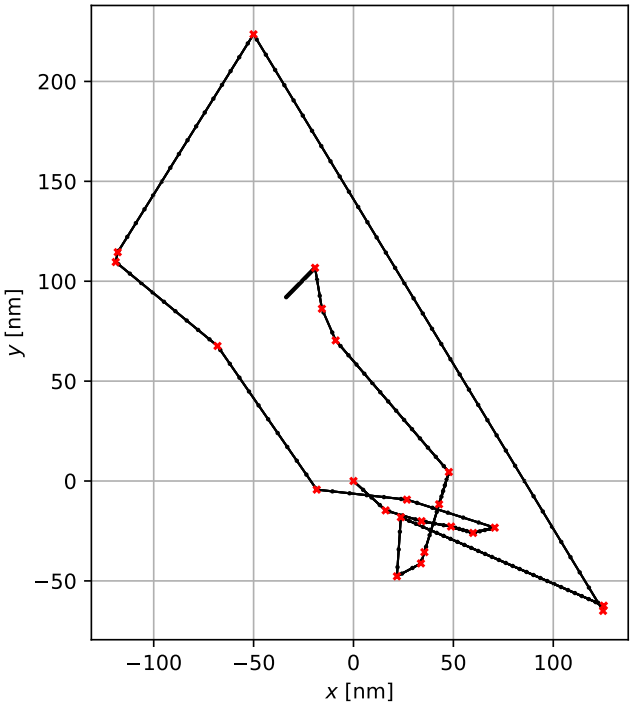

Figure 6: One sampled electron moving through the semiconductor with no applied field.

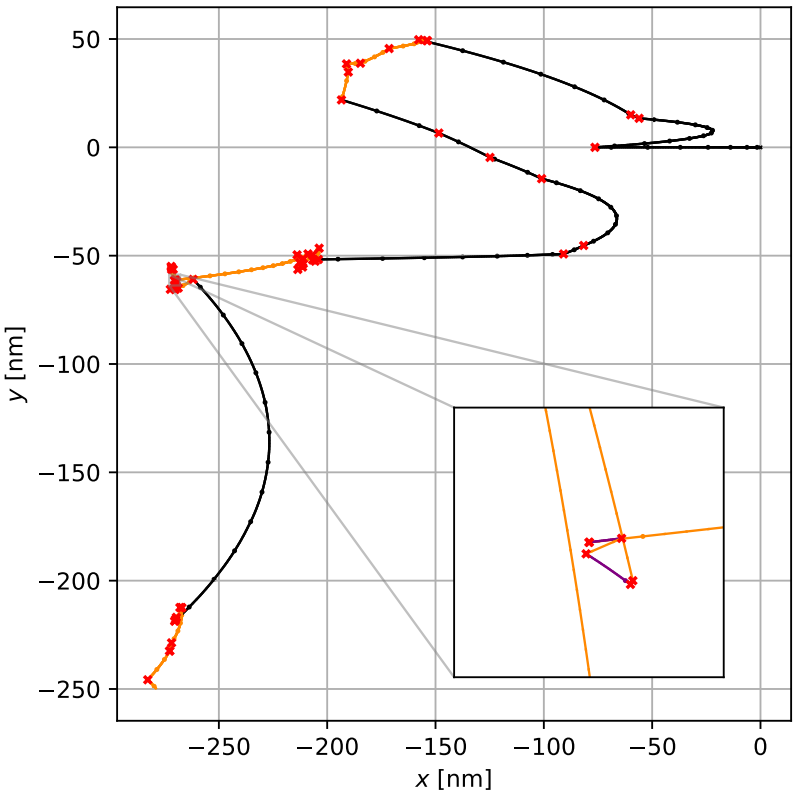

Figure 7: One sampled electron moving through the semiconductor with an external field of $\mathbb{E}_x = 30$ kV/cm.

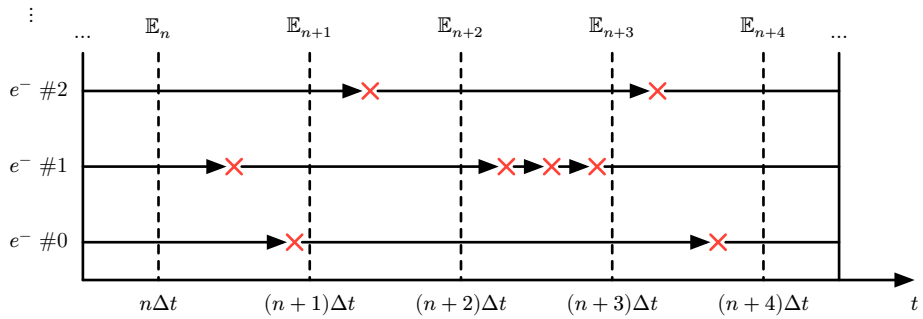

Figure 8: Qualitative diagram of how scatterings can happen in time for a multitude of electrons. Free flights are indicated with black arrows, scattering events with red crosses.

3.3. Multi-particle device simulation

For simulating devices, multiple electrons are simulated together in an ensemble system. As the carriers excite the electric field, they accelerate each other through the Coloumb force and as such the electric field needs to be tracked over space and time. Additionally, the multi-particle simulation has a defined device geometry, where the properties of the material change in space. The simulator in this work is a one-dimensional simulator, as such the space is discretized into a one-dimensional grid, storing both the properties of the material and the value of the electric field, described in detail in Section 3.3.1.

The electric field $\mathbb{E}$ needs to be solved at a rate faster than the half of the angular plasma oscillation frequency of the semiconductor ω_p to avoid instability [5]. In this work, the electric field is solved in time steps of 5 fs, orders of magnitude faster than the plasma oscillation frequency of GaAs.

As illustrated in Figure 8, the electrons may scatter multiple times in the middle of a time step and may not be synchronized with each other nor synchronized with the time steps. The iteration scheme in the Monte Carlo method in this work is described as follows:

1. Count the number of charges per cell, both from carriers and ionized impurities. See Section 3.3.1.
2. Update the solution of electric field $\mathbb{E}$ based on this charge distribution. See Section 3.3.1.
3. For each electron in the system,
   - If the electron has reached any boundary of the simulation domain, handle the boundary condition accordingly. See Section 3.3.4.
   - If the electron's current free flight ends after the current time step Δt ends, let it experience free flight until the end of the time step. Adjust the electron's remaining free flight time accordingly and move on to the next electron.

- Otherwise, let the electron experience free flight for the remaining time it has until it is set to scatter. Let the electron experience a scattering event and sample the new remaining time in free flight.
- Repeat from step 2 for this electron.

4. Sample all the statistical properties being recorded for this run.
5. Increase the simulation time by Δt. Repeat from step 1 if whatever stopping condition defined for this problem has not been reached.

3.3.1. Discretization and electric fields

Gauss' law for the electric field in integral form states that, for any volume V with charge density ρ_V:

$$\oint_{\partial V} \varepsilon \vec{\mathbb{E}} \cdot \hat{n} \, \mathrm{d}A = \int_V \rho_V \, \mathrm{d}V. \tag{34}$$

As a quasi-static approximation is made, the electric field is a conservative field, meaning the electric potential $\mathbb{V}$ is well defined:

$$\mathbb{V}(\vec{r}) - \mathbb{V}(\vec{r_0}) = -\int_{\vec{r_0}}^{\vec{r}} \vec{\mathbb{E}} \cdot \hat{l} \, \mathrm{d}l. \tag{35}$$

For the Schottky barrier diode, the space is discretized into a one-dimensional line of N cells, each of longitudunal length Δx and cross-sectional area A as shown in Figure 9. The cells are indexed such that the first cell is numbered as $i = 0$ and the last cell as $i = N - 1$. Each cell is assumed to have a constant ε taken as the permittivity of the material in the cell. The volume charge density ρ_V is determined by counting the number of donors and the number of carriers inside each cell.

The coordinate system along the x-axis is set up such that the Schottky barrier is located at $x = 0$ and the ohmic contact is located at $x = L_x = N\Delta x$, with cell i spanning the space between $[i\Delta x, (i+1)\Delta x]$.

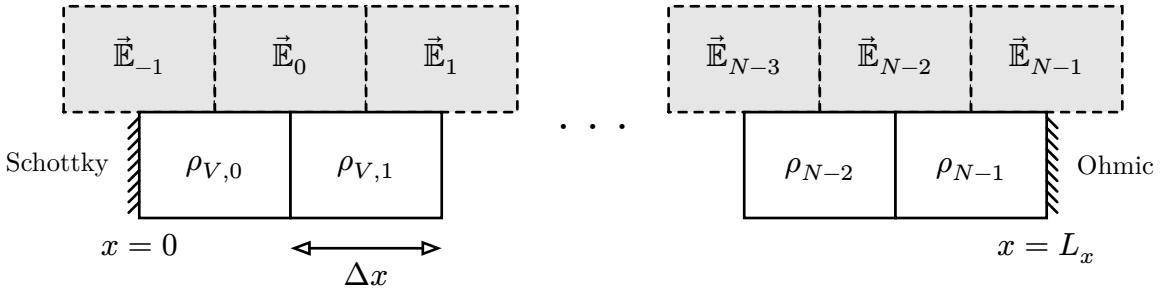

Figure 9: Diagram of the discretization of the system. The first line shows the half-grid $\vec{E}$-field, the second shows the whole grid density of charge

The electric field $\mathbb{E}$ is discretized in the half-grid between the cells, such that $\mathbb{E}_i$ is centered at $(i+1)\Delta x$, ranging from $\left[\left(i+\frac{1}{2}\right)\Delta x, \left(i+\frac{3}{2}\right)\Delta x\right)]$. The electric field is assumed constant within each half-grid cell, and assumed to only point longitudunally, $\vec{\mathbb{E}} = \hat{x}\mathbb{E}_x$.

To solve the electric field given the volume charges, eq. 34 is applied for each cell volume V_i

$$\begin{aligned} \oint_{\partial V_i} \varepsilon_0 \varepsilon_r \mathbb{E}\, \mathrm{d}S &= \int_{V_i} \rho_V \, \mathrm{d}V \\ A\varepsilon_0\varepsilon_r\left(\mathbb{E}_{x,i} - \mathbb{E}_{x,i-1}\right) &= A\Delta x \rho_{V,i} \\ \mathbb{E}_{x,i} - \mathbb{E}_{x,i-1} &= \Delta x \frac{\rho_{V,i}}{\varepsilon_0\varepsilon_r}. \end{aligned} \tag{36}$$

3.3.2. Boundary conditions

Both the Schottky contact and the ohmic contact have a surface charge $\rho_{S,\text{Schottky}}$ and $\rho_{S,\text{ohmic}}$. The total surface charge is known from conservation of charge, but the exact charge on each surface is not known. To solve the electric field and the surface charges exactly, three boundary conditions are used:

$$\begin{aligned} \text{Surface charge on Schottky: } \mathbb{E}_{x,-1} &= \frac{\rho_{S,\text{Schottky}}}{\varepsilon_0\varepsilon_r} \\ \text{Surface charge on ohmic: } \mathbb{E}_{x,N-1} &= -\frac{\rho_{S,\text{ohmic}}}{\varepsilon_0\varepsilon_r} \\ \text{Voltage applied: } \mathbb{V}(x=L_x) - \mathbb{V}(x=0) &= \mathbb{V}_{\text{ext}} \end{aligned} \tag{37}$$

The left-hand side of the last boundary condition is evaluated as

$$\begin{aligned} \mathbb{V}(x=L_x) - \mathbb{V}(x=0) &= -\int_{x=0}^{x=L_x} \vec{\mathbb{E}} \cdot \hat{l}\, \mathrm{d}l = \\ &= -\int_{x=0}^{x=L_x} \mathbb{E}_x \, \mathrm{d}l = -\Delta x \left[\sum_{i=0}^{N-2} \mathbb{E}_{x,i} + \frac{1}{2}\left(\mathbb{E}_{x,-1} + \mathbb{E}_{x,N-1}\right)\right] \end{aligned} \tag{38}$$

With $N+3$ unknowns ($N+1$ electric field elements and two surface charges) and $N+3$ equations (N equations from eq. 36, three boundary conditions), this forms a solvable linear system of equations giving an unique solution for the electric field and surface charges.

3.3.3. Superparticles

The total number of electrons in the system is $n_{\text{tot}} = \sum_{i=0}^{N-1} A\Delta x N_{D,i}$, $N_{D,i}$ being the donor volume density of cell i. This full number of electrons can be prohibitively large to simulate, even on modern supercomputer hardware. Instead, we

choose to simulate a sample of n_{sp} electrons out of the n_{tot} electrons where each one of these simulated electrons, called a "superparticle" [8], represents $f = \frac{n_{\text{tot}}}{n_{\text{sp}}}$ physical electrons, called the "superparticle factor". As each superparticle represents f electrons, the charge of such a superparticle is taken as $-fq_0$.

The charge density $\rho_{V,i}$ of a cell i has contributions from the negative electrons inside the cell and the positively ionized donors. For a donor concentration $N_{D,i}$, the total charge of the ionized donors is $q_0 A\Delta x N_{D,i}$. For a number $n_{\text{sp},i}$ of superparticles inside the cell, the total charge of the superparticles is $-q_0 f n_{\text{sp},i}$. Thus the total volume charge density inside the cell is

$$\begin{aligned}\rho_{V,i} &= \frac{1}{A\Delta x}\left[q_0 A\Delta x N_{D,i} - q_0 f n_{\text{sp},i}\right] \\ &= q_0\left[N_{D,i} - \frac{f n_{\text{sp},i}}{A\Delta x}\right]\end{aligned} \tag{39}$$

To accurately estimate n_{sp}, each particle is assigned to its two most nearby cells, with each cell being given a fractional amount of the charge according to how close the particle is to ecah cell. If a particle is located between cell $i-1$ and i at position $r_x = \Delta x(i+\delta), -\frac{1}{2} < \delta < \frac{1}{2}$, then for this particle $n_{\text{sp},i-1}$ is $-\delta + \frac{1}{2}$ and $n_{\text{sp},i}$ is $\delta + \frac{1}{2}$. This means a particle located exactly at the center of a cell will contribute only to that cell, while a particle right between two cells will contribute to the two cells equally.

For all devices simulated, $n_{\text{sp}} = 10000$.

3.3.4. Schottky and ohmic contacts

As described in Section 2.3.1, metal-semiconductor contacts can, depending on whether thermionic emission or quantum tunneling dominates, be classified as either a Schottky contact or ohmic contact. For electrons inside the semiconductor, the contacts are treated the same: since the electron's energy is higher than the Fermi level of the metal, they are free to move from semiconductor to metal and any electron leaving the semiconductor is removed from the simulation domain.

Instead of simulating the quantum tunneling behaviour of the electrons for the ohmic contact, the method from in [8] is followed: an ideal (meaning zero-resistance) ohmic contact can locally be treated as a system in thermal equilibrium, over which no voltage drop is present. Such a system can be realized by maintaining a neutrally charged region close to the ohmic contact. The simulator implements such a system by, at each time step, calculating the total charge within a distance Δx_{ohmic} of the ohmic contact, injecting a number of electrons into the ohmic contact to neutralize this charge. The simulator cannot neutralize

a situation where there are too many electrons in the system, but such a situation should not happen at the ohmic contact in the systems simulated.

For the Schottky contact thermionic emission is assumed to dominate and as such tunneling is considered negligible and not simulated. As mentioned in Section 2.3.1, in the thermionic emission model the current injected from the metal into the semiconductor $J_{\text{met.} \to \text{s.c.}}$ is constant, depending only on the temperature T and Richardsson constant A^* by eq. 18. At each time step Δt of the simulation, the number of expected superparticles that enter the computational domain from the Schottky contact is $\frac{1}{q_0}\frac{1}{f}A\Delta t J_{\text{met.} \to \text{s.c.}}$. The simulator injects this number of electrons on average, sampling from an exponential distribution to inject each particle at a random instant.

An electron with x-component of its velocity facing out of the semiconductor would be immediately re-absorbed by the metal. As such, all injected electrons have the x-component of its velocity facing into the semiconductor. The electrons are otherwise in thermal equilibrium with the lattice.

3.3.5. Simulations performed

To validate the simulation of the Schottky barrier diode, models of a number of diodes fabricated and measured at the Chalmers Terahertz and Millimetre Wave Laboratory were simulated and data was compared to the measured values for the fabricated diodes. The diodes are made in GaAs with Ti/Pd/Au Schottky contacts and Pd/Ge/Au/Pd/Au ohmic contacts. Details about the devices are listed in Table 2. The barrier height is estimated to be 0.75 V.

The experimental data consists of IV-curves, where the current is recorded as the voltage is swept. The measured diodes are connected in an anti-parallel configuration, where two identical diodes are connected anode-to-cathode and

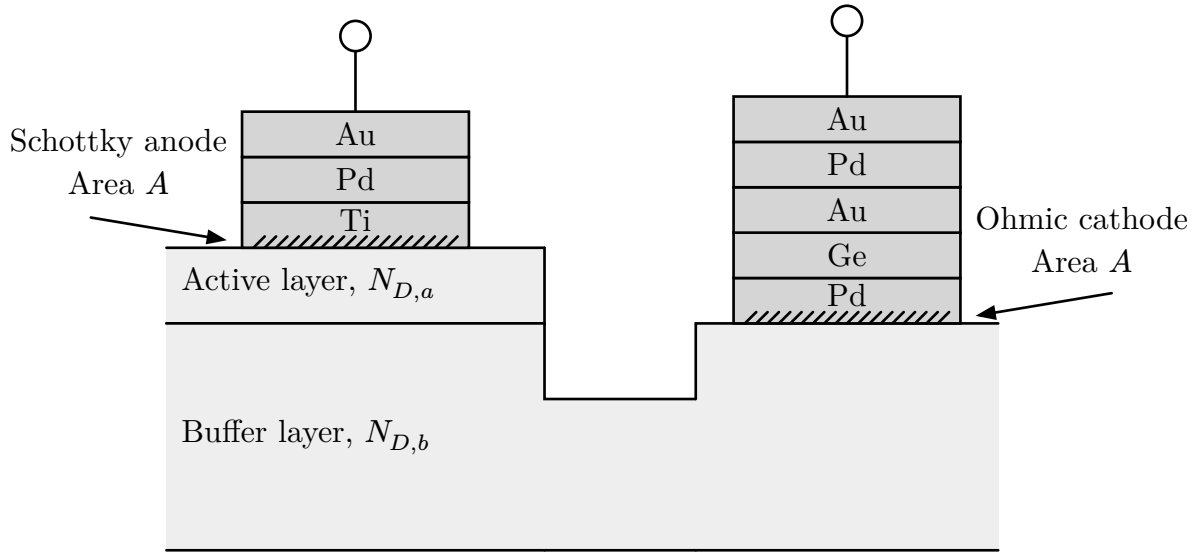

Figure 10: Diagram of the physical layout of the diode

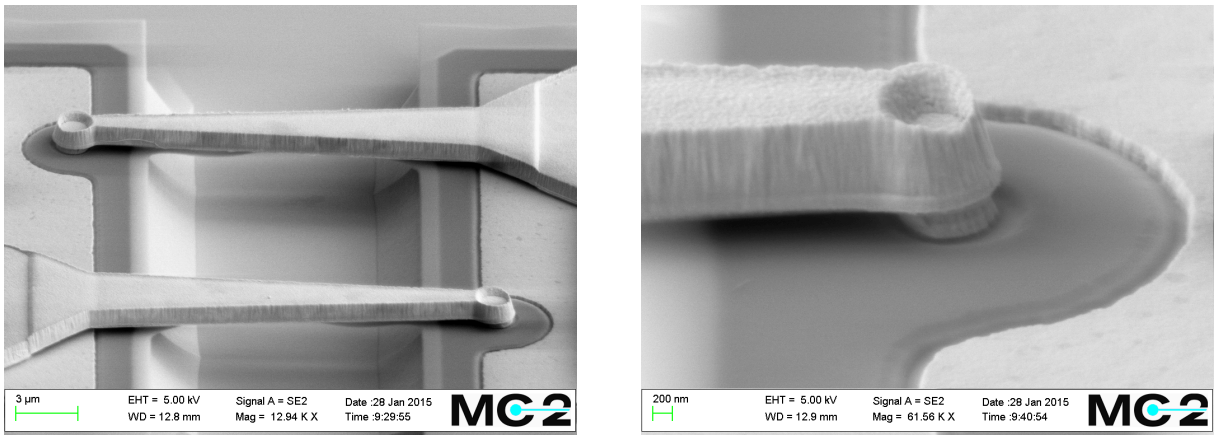

Figure 11: SEM-micrograph of a fabricated antiparallel device and of one individual Schottky contact

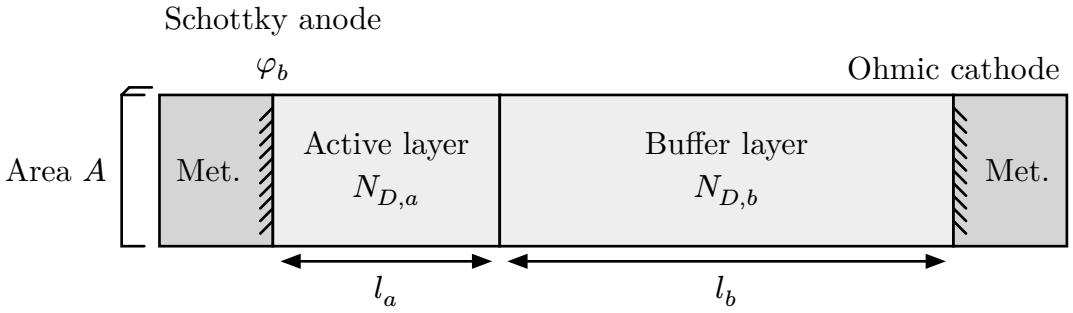

Figure 12: One-dimensional approximation used, with parameters indicated

cathode-to-anode. At a positive voltage, the current from the conducting diode strongly over-powers the small current from the non-conducting diode. Therefore, only data points for the diode at strongly positive bias is used. For this work, the author judged a lower limit of 0.4 V to be sufficient for treating the non-conducting diode as negligible. The endpoint of the voltage sweep is 1 V, however the current measurement instrument cannot measure currents stronger than 10 mA. Any datapoint with a current reaching this instrument limit is discarded.

3.3.5.1. Estimating saturation current, ideality factor and series resistance

For both the simulated and measured IV-curves, the diode equation with a series resistance in eq. 22 is fit against the data, where the saturation current I_0, ideality factor n and series R_s are fit using a least squares algorithm to give an indication

Device name	$A[\mu m^2]$	φ_b [mV]	$N_{D,a}$ [cm^{-3}]	l_a [nm]	$N_{D,b}$ [cm^{-3}]	l_b [nm]
AB-3.2	3.2	750	$5.0 \cdot 10^{17}$	48	$5.0 \cdot 10^{19}$	2500
AB-0.44	0.44	750	$5.0 \cdot 10^{17}$	48	$5.0 \cdot 10^{19}$	2500
AI-0.8	0.8	750	$3.0 \cdot 10^{17}$	60	$5.0 \cdot 10^{19}$	2500

Table 2: Parameters for the diodes measured.

of how accurate the simulation is compared to the measurement. To perform the linear fit for high voltages ($\mathbb{V}_{\text{ext}} \gg \frac{k_B T}{q_0}$), we rewrite

$$\begin{aligned} I_d &= I_0 \left(\exp\left(\frac{q_0}{n k_B T} (\mathbb{V}_{\text{ext}} - R_s I_d) \right) - 1 \right) \\ &\approx I_0 \exp\left(\frac{q_0}{n k_B T} (\mathbb{V}_{\text{ext}} - R_s I_d) \right) \\ \ln I_d &= \ln I_0 + \frac{q_0}{n k_B T} \mathbb{V}_{\text{ext}} - \frac{R_s q_0}{n k_B T} I_d \end{aligned} \tag{40}$$

which is a linear system in terms of $\ln I_0$, $\frac{q_0}{n k_B T}$ and $\frac{R_s q_0}{n k_B T}$, which is fitted with a linear least squares algorithm to the datapoints $\{(\mathbb{V}_{\text{ext}}, I_d)\}$, from which I_0, n and R_s are solved.

3.3.5.2. Estimating diode capacitance

No charge-voltage (QV) measurements nor capacitance-voltage (CV) measurements were available for the manufactured diodes. Instead, the capacitance predicted by the simulation is compared against the capacitance predicted by the ideal diode model. From Section 2.3 eq. 15, the relation between the surface charge ρ_s on the Schottky contact and the applied voltage $\mathbb{V}_{\text{ext}}$ can be found as

$$\rho_s(\mathbb{V}_{\text{ext}}) = -\sqrt{2 q_0 N_D \varepsilon (\varphi_{\text{bi}} - \mathbb{V}_{\text{ext}})}. \tag{41}$$

The capacitance of the diode is then

$$\begin{aligned} C(V) = \frac{\mathrm{d}Q}{\mathrm{d}\mathbb{V}_{\text{ext}}} &= A \frac{\mathrm{d}\rho_s}{\mathrm{d}\mathbb{V}_{\text{ext}}} = \\ &= A \sqrt{\frac{\varepsilon q_0 N_D}{2\varphi_{\text{bi}} - \mathbb{V}_{\text{ext}}}} = \\ &= \frac{C(V=0)}{\sqrt{\varphi_{\text{bi}} - \mathbb{V}_{\text{ext}}}}. \end{aligned} \tag{42}$$

To predict the capacitance from the simulator, at each voltage level, the total surface charge $\rho_s = \rho_{s,\text{Schottky}} + \rho_{s,\text{ohmic}}$ is recorded. $C(V) = \frac{\mathrm{d}Q}{\mathrm{d}\mathbb{V}_{\text{ext}}}$ is numerically estimated using a finite difference method and $C(V=0)$ is estimated by taking the mean of $C(V)\sqrt{\varphi_{\text{bi}} - \mathbb{V}_{\text{ext}}}$ for the voltage levels recorded. No data is used for $\mathbb{V}_{\text{ext}} > \varphi_{\text{bi}}$ since the capacitance is not well-defined above the built-in voltage.

3.4. Computational implementation details

The simulator is implemented in the Rust programming language, designed to run in a multi-core environment. The single-particle simulator runs in parallel on all available cores, averaging all statistical results after each core has finished

running. For the multi-particle Monte Carlo simulator, all but one core are utilized to simulate the scatters and free flights of all electrons, which are divided equally among the cores. The remaining core solves the electric field in accordance with Section 3.3.1, and manages all other cores to ensure the simulation stays synchronized. Solving Poisson's equation, plus synchronizing all cores has been measured to take about 2% of the total computation time, the remaining time utilized simulating the electrons. The multi-particle simulation runs at approximately 2 simulated picoseconds per wall second, or about -117 dBs/s.

All simulations are run on the C3SE Vera computer cluster. When generating IV-curves, the voltage sweep is performed in parallel over many machines.

The code for the simulator is available online at the following URL:
`https://github.com/xeniagda/gambling-simulator`

4. Results

In this chapter the experiments described in Sections 3.2.1 and 3.3.5 are performed and the results are described. All results are for GaAs at room temperature $T = 300$ K. For single-particle simulations, the doping concentration is 10^{15}cm^{-3}.

4.1. Single-particle Monte Carlo

In Figure 13, simulated data for the mean velocity and mobility against field strength is compared against the measured data from [27] and the model in [28]. The plots shows good agreement for both the value of the low-field mobility, the critical field strength and the saturated velocity.

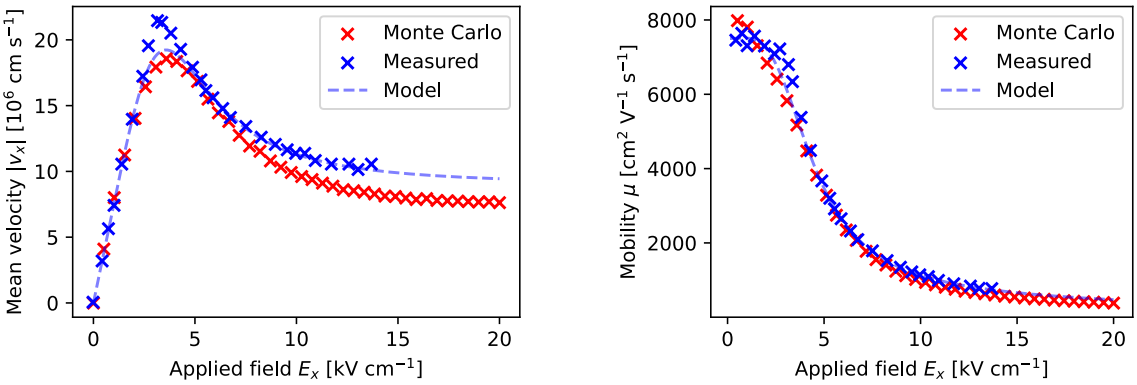

Figure 13: Mean electron velocity and mobility μ against field strength. Results from simulation, measured data from [27] and model from [28] are shown.

In Figure 14, the valley occupancy and the mean electron effective mass is shown against field strength. As expected, Figure 14 show as the applied field strength is increased more electrons move to the L-valley and the X-valley, and as more electrons enter the L-valley, the effective electron mass m^* increases, impeding acceleration from the electric field.

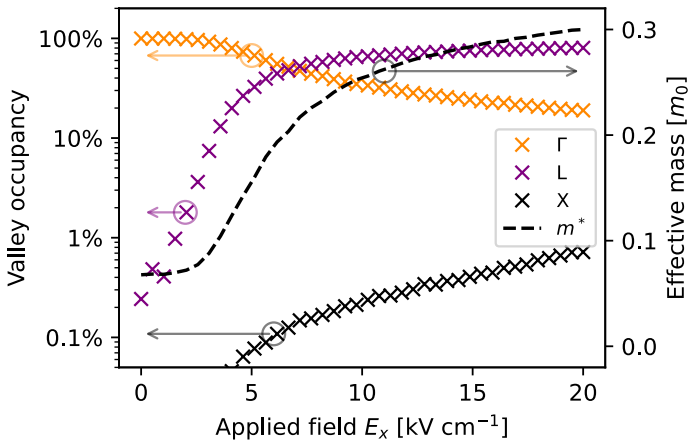

Figure 14: Valleys occupied by electrons at different field strengths.

In Figure 15, the diffusion coefficient is shown against field strength, compared to the Einstein relation and a previous Monte Carlo study of the diffusion coefficient in [29]. The diffusion coefficient matches the reference well.

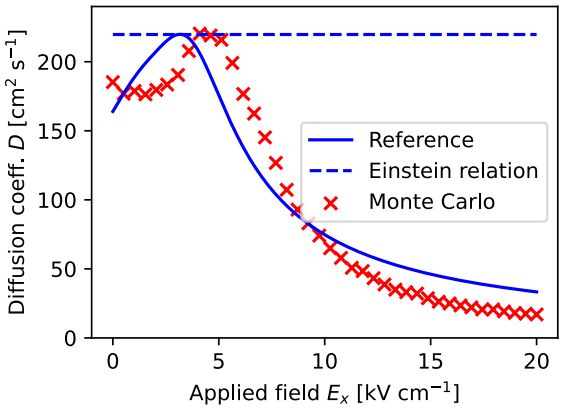

Figure 15: Diffusion coefficient against field stregnth. Results from simulation, results from [29] and low-field coefficient from the Einstein relation are shown.

In Figure 16 the rate of each individual type of mechanism is shown for different field strengths. As can be seen, intravalley optical scattering and impurity scattering dominate at low field strength, agreeing with [17]. At higher field strengths, intervalley optical phonon scattering in the L-valley dominates, in line with how in Figure 14 the majority of electrons enter the L-valley.

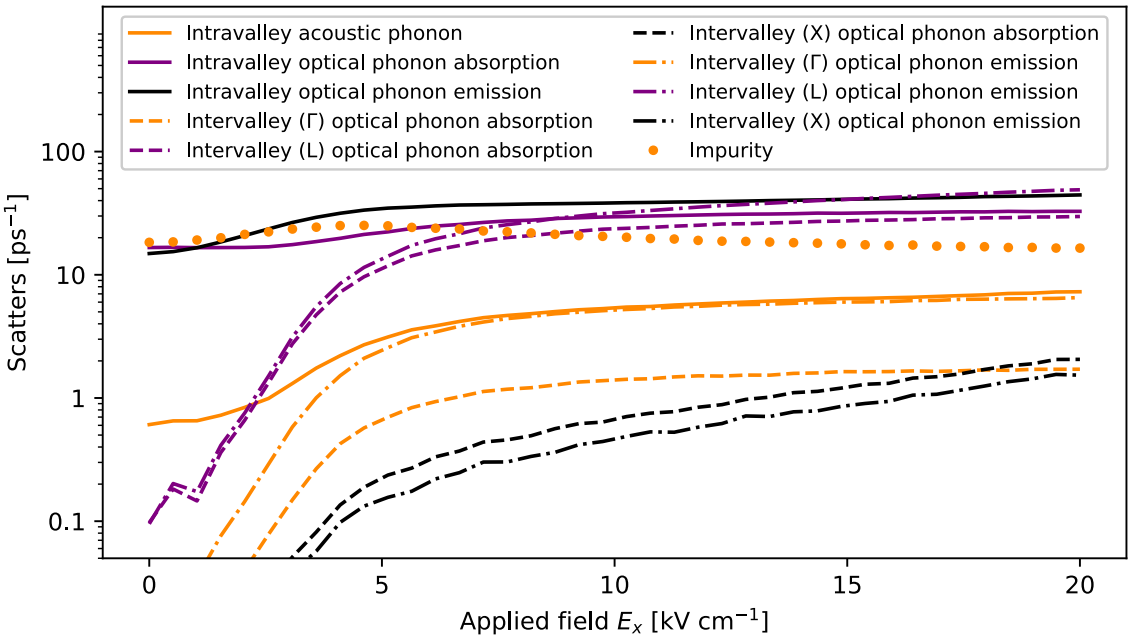

Figure 16: Rate of scattering mechanism at different field strengths.

4.2. Multi-particle Monte Carlo

In Figure 17 a, c, e) the IV-curves for the three measured and simulated diodes are shown, both being fitted to the non-ideal diode equation with series resistance as described in Section 3.3.5.1. In Figure 17 b, d, f) the charge and capacitance against voltage is shown for the simulated diodes and predicted by the ideal diode equation.

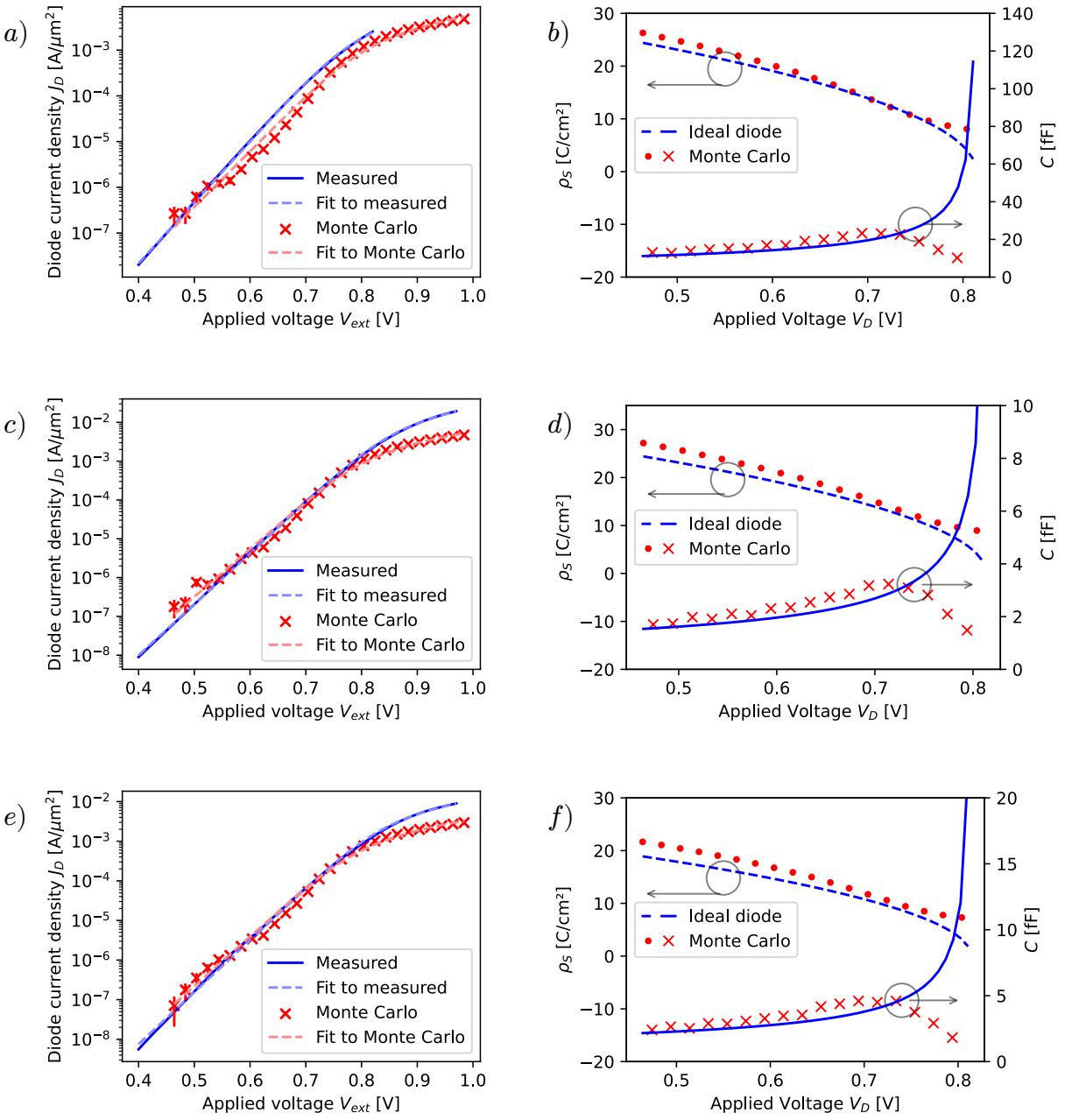

Figure 17: IV and QCV-curves for measured, simulated and ideal diodes. AB-3.2 is shown in a, b), AB-0.44 is shown in c, d), AI-0.8 is shown in e, f).

In Figure 18, the electric field $\mathbb{E}$, the electric potential $\mathbb{V}$ and charge density ρ_V are shown over the diode AB-3.2 at different forward voltages. To reduce visual noise, a rolling average of the volume charge is also shown. The width of the depletion region x_d as predicted by the ideal diode model is indicated.

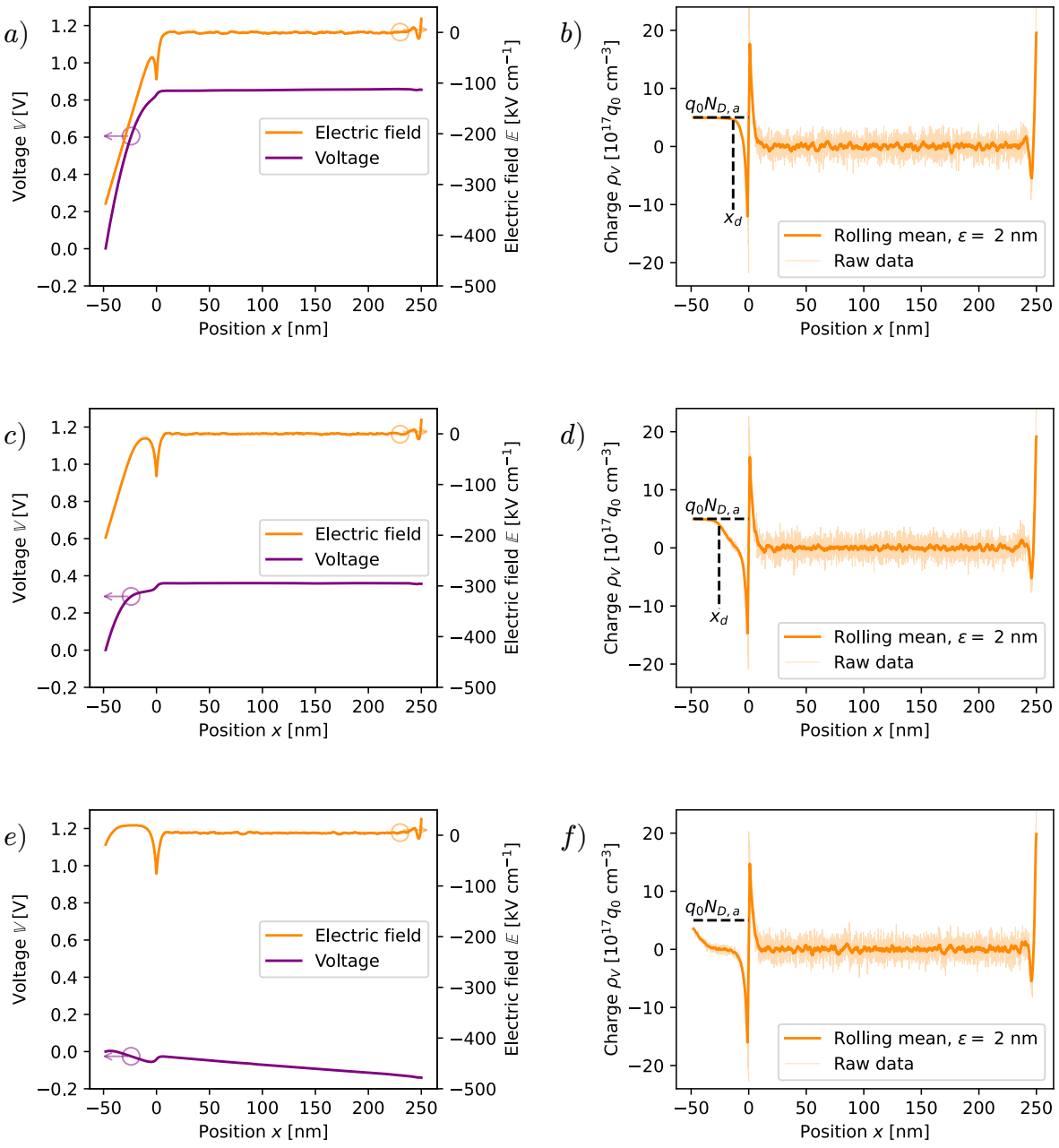

Figure 18: Electric field $\mathbb{E}$, potential $\mathbb{V}$ and charge density ρ_V over the diode AB-3.2[(2)]. The active region and buffer region meet at $x = 0$.
$\mathbb{V}_{\text{ext}} = 0$ V is shown in a, b), $\mathbb{V}_{\text{ext}} = 0.5$ V is shown in c, d), $\mathbb{V}_{\text{ext}} = 1.0$ V is shown in e, f).

[(2)]To aid in visually discerning the active region of the diode, the buffer layer has been shrunk to 250 nm. To minimize the impact on the behaviour of the device, the doping level is decreased accordingly, meaning the resistance of the buffer region is kept the same.

In Table 3 the extracted saturation current I_{sat}, ideality factor n and series resistance R_s are listed for all the simulated and measured diodes, and the zero-voltage capacitane is extracted from the simulation and predicted from the ideal diode.

Diode	**Kind**	I_{sat} [fA]	n [−]	R_s [Ω]	$C(V=0)$ [fF]
AB-3.2	Measured	334	1.26	5.20[(3)]	-
	Ideal	-			7.32
	Monte Carlo	942	1.38	8.38	7.55
AB-0.44	Measured	24.6	1.28	10.9	-
	Ideal	-			1.01
	Monte Carlo	97.2	1.36	61.6	1.04
AI-0.8	Measured	43.6	1.28	11.9	-
	Ideal	-			1.42
	Monte Carlo	120	1.34	46.6	1.49

Table 3: Extracted parameters for all diodes, measured, ideal and Monte Carlo

[(3)] The current at high voltage for AB-3.2 exceeds the 10 mA limit of the current measurement instrument before the series resistance becomes significant, as can be seen in Figure 17 *a*). This may mean the resistance as predicted by the least-squares method might not be as accurate for this diode as for the other diodes.

In Figure 19, the electron velocity distribution is shown at the Schottky contact. In Figure 20 the electron energy is shown in the middle of the buffer region. Both figures show the distribution for the electrons in all valleys, and for the electrons in each individual valley. The energy distribution is additionally shown for the Maxwell-Boltzmann distribution.

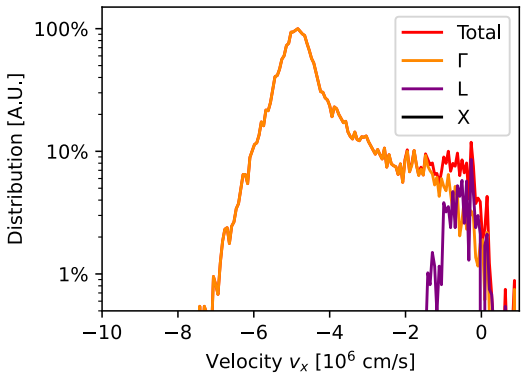

Figure 19: Velocity distribution at the Schottky contact

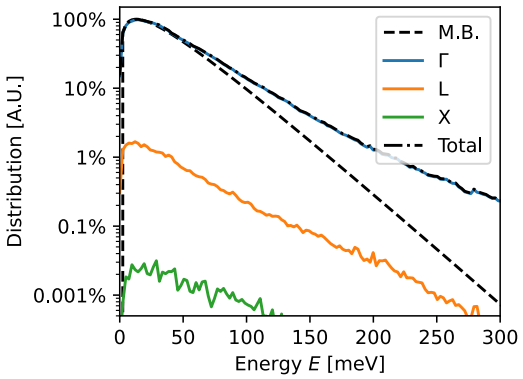

Figure 20: Energy distribution inside buffer region at $\mathbb{V}_{\text{ext}} = 1.0$ V.

In Figure 21, the electron temperature (as defined by the mean value of the energy distribution) is indicated at all points in the diode at different applied voltages. As with the charge distribution, a rolling average is been applied.

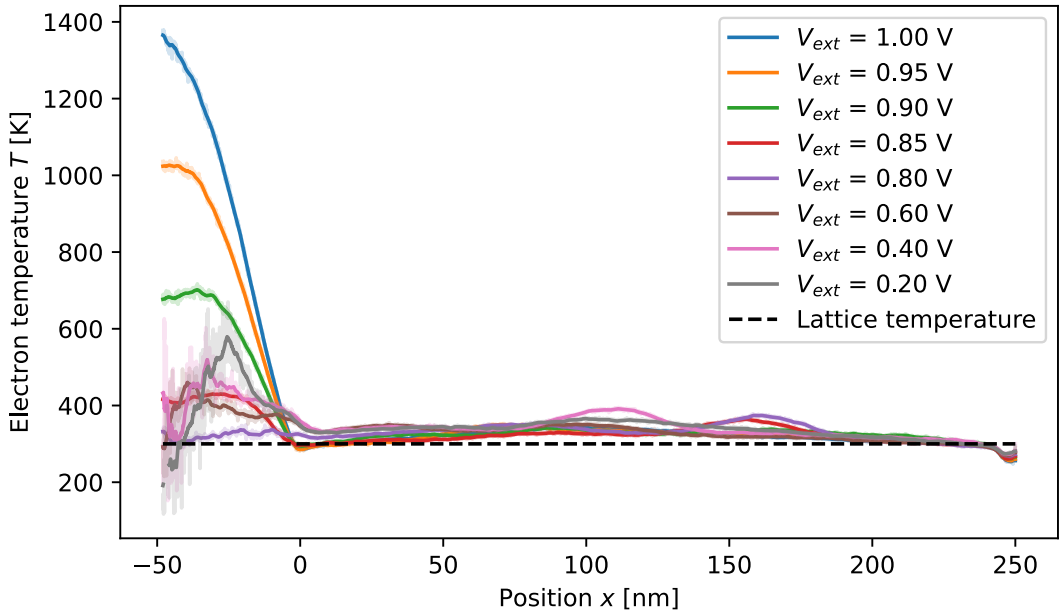

Figure 21: Electron temperature over the diode at different voltages. The active region and buffer region meets at $x = 0$.

5. Discussion

5.1. Charge distribution

As visible in the volume charge density ρ_v plots in Figure 17 b, d, f), the ohmic contacts show a charge dipole building up by the metal before returning to equilibrium inside the buffer region. The magnitude of the charge dipoles seem to have a slightly positive dependence on the applied voltage. Due to the small extent in space of the charge dipole, the impact on the voltage drop is rather small and should have relatively low impact on the overall characteristics on the device.

This charge dipole is characteristic of this approach for treating ohmic contacts. In [30], a number of different approaches, including the one used in this work, are compared. The approach used in this work gives a very similar charge dipole in their simulations.

As seen in Figure 17 b, d), the simulated depletion region has a width that follows the theoretical model well. In Figure 17 b, d), at $\mathbb{V}_{\text{ext}} = 1.0$, the potential over the junction is negative and no depletion region is predicted to exist. Indeed the active region is not fully depleted even next to the Schottky contact.

5.2. Current-voltage relationship

While the saturation current in Table 3 varies by a factor of up to 3 and beyond between simulation and measurements, this is compensated for by a slight over-estimation in ideality factor, meaning the current before series resistance dominates is quite well-predicted by the simulation, as can be seen in Figure 17 $a - c$). The simulator over-estimates the series resistance, meaning the current at high voltage is quite severely under-estimated by the simulator.

This over-estimation in resistance could depend on a multitude of factors. One reason could be due to the carriers experiencing such a high field in the depletion region (on the order of 300 kV/cm, which Figure 18 a) reaches). Here, they could happen to enter a valley not modelled by this simulator. In [31], the X^7 and Γ^7 -valleys are simulated in addition to the Γ, L and X-valleys[(4)], and at such high fields a large amount of electrons reside in the X^7-valley. The X^7-valley does have a lower effective mass than the X-valley, increasing the drift velocity at these field strengths, which could potentially result in a lower resistance of the depletion region.

Another reason for the under-estimation of the resistance of the diode could be due to the one-dimensional approximation of the geometry. The true diode is

[(4)] As previously mentioned, what we in this work call the Γ-, X- and L-valleys are the Γ^6-, X^6- and L^6-valleys.

hemicylindrically shaped, with the Schottky contact at the center, ohmic contact further out, the effective area of the ohmic contact is a lot larger than the area of the Schottky contact. In the simulation the area of the one-dimensional diode is taken as the Schottky contact area, constant over the whole structure. As such, the buffer layer and ohmic contact would have a lot higher resistance in the simulation than reality.

Lastly, the high resistance of the simulated device could be due to Pauli's exclusion principle not being taken into account. As Pauli's exclusion principle prevents electrons from scattering into a state that is already occupied, it is typically [11] modelled by reducing the scattering probability by a factor $1 - f\left(\vec{r'}, \vec{k'}\right)$, where $f\left(\vec{r}, \vec{k}\right)$ is the distribution function of the electrons. As degeneracy in GaAs at 300K is expected to play a role at a carrier concentration of $> 5 \times 10^{17}\text{cm}^{-3}$, the effect is less pronounced in the active layer and more pronounced in the buffer layer. Taking Pauli's exclusion principle into account would therefore lower the scattering rate in the buffer layer, meaning the electrons on average have higher energy and velocity, lowering the effective resistance of the region.

5.3. Capacitance-voltage relationship

The surface charge and the capacitance follows the ideal diode well for lower voltages, but as $\mathbb{V}_{\text{ext}}$ approaches φ_{bi} the surface charge deviates from the ideal diode and the capacitance is quite severely under-predicted. Nevertheless, the mean capacitance value extrapolated to $\mathbb{V}_{\text{ext}} = 0$ is within a few percent of the theory.

While the value for capacitance match well between the simulation and theory, they are both based on the same one-dimensional geometrical approximation. In the manufactured diode, fringing fields may extend between the active layer and the ohmic contact, and other edge-effects have a large impact on the capacitance. In [32] a Schottky barrier diode with a similar device structure is investigated, where the geometry is approximated by a 2-dimensional grid. From their results, the 2-dimensional diode may have up to 4 times the capacitance than the one-dimensional approximation. With this in mind, we do not expect the results regarding capacitance in this work to be very accurate compared to reality.

5.4. Electron temperature and velocity distribution

As seen in Figure 21, the electron temperature remains in equilibrium with the lattice in the buffer layer and increases in the active region as the voltage increases, matching the results shown in [6]. Additionally, as seen in Figure 19, a significant number of electrons reside in the L-valley at the Schottky contact. The electrons in the Γ- and L-valleys show very different velocity distributions,

indicating a presence of intervalley noise. While no direct noise measurements were done in this work, the values for the active layer electron temperature and the characteristics for intervalley scattering in the active layer could be used with the approach in [7] to predict the noise characteristics of the diode.

6. Conclusions and future work

The transport properties predicted by the single-particle simulation show good agreement to literature values of previous measurements and simulations.

In the multi-particle simulator, the current-voltage relationship is predicted well by the simulator at low voltages. Due to the over-estimation of the series resistance the current is under-predicted at higher voltages. The simulated capacitance matches the theory well; however neither the simulation results nor the theoretical capacitance is expected to match the fabricated device well due both being based on a one-dimensional model of the diode which does not take edge-effects into account. As the capacitance and series resistance of the diode both play a big role in the high-frequency behaviour of the device, the results of this work are not sufficient to accurately model diodes for use at THz devices such as mixers, detectors or frequency multipliers. A number of improvements could be made to make the simulator more accurate and useful at high frequencies.

As mentioned in Section 5.2 and Section 5.3, both the over-estimation of the resistance and the inaccuracies in the capacitance can be improved by modelling the geometry of the device better. A 2-dimensional approach like the one presented in [32] could be used to capture the edge effects: however for the 2-dimensional diode the effect of the area of the ohmic contact being larger than the Schottky contact would not be properly captured. While a full 3-dimensional approach could work, a cylindrical coordinate system, with the Schottky contact at the center of the rotational axes could also represent the diode well. In such a geometry, radial symmetry could be assumed, making the simulator effectively have a two-dimensional simulation domain. Such a geometry is sketched in Figure 22 and would capture both edge effects and the difference in area between the inner Schottky contact and the larger buffer region and ohmic contact.

To solve Poisson's equation in either a 2-dimensional or radially-symmetric cylindrical geometry, a more sophisticated approach than the explicit method presented in Section 3.3.1 must be used. One may discretize the equation with finite differences and write it in matrix form, after which a matrix solver may be used. However, even if one pre-computes the inverse of the matrix, this still needs N^2 operations where N is the number of cells in the grid, meaning this approach could be prohibitively slow. A number of more sophisticated methods are presented in [11]. A Fourier-based method may be used instead, where the solution is assumed to be a sum of eigenfunctions consisting of sines and cosines, which allows us to compute the solution a lot faster; however, this is only directly applicable to simulations domains which are discretized into regular square grids, and as such is not directly applicable to the proposed cylindrical domain. For this domain, an iterative approach could be useful. An exact solution

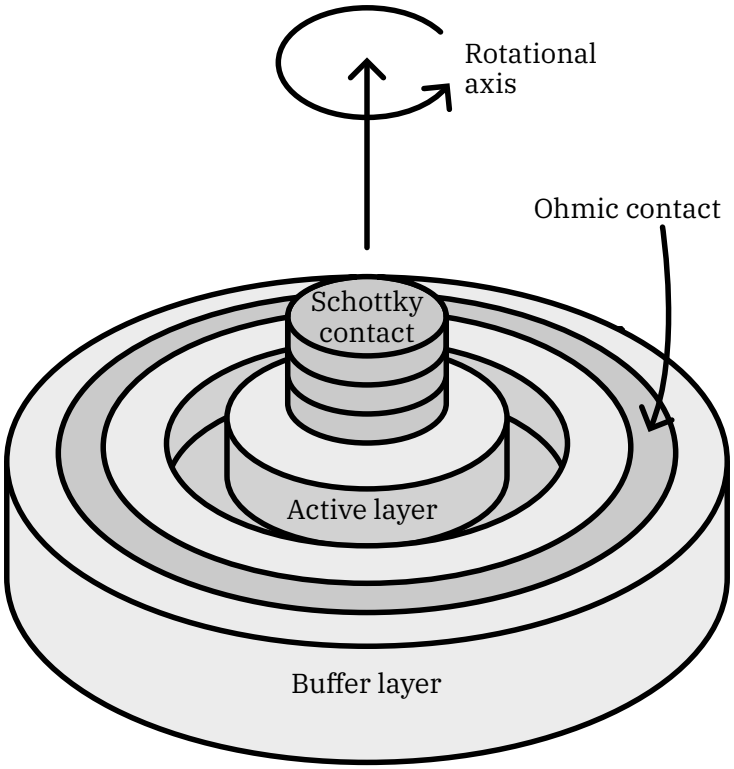

Figure 22: Possible cylindrical geometry for the Schottky barrier diode

to Poisson's equation is not computed each step, but instead a computationally cheaper inexact solution based on the previous solution is computed. Iterating this approach converges to an exact solution, however can result in instabilities if the convergence is slower than the movement of the charges.

As mentioned in Section 5.1, there is a charge dipole building up at the ohmic contacts, causing the device not to be in local equilibrium at the contact and causing a small voltage drop over it. In [30] a number of different physical models for ohmic contacts are presented and compared. For the Schottky barrier diode, the velocity-weighted Maxwell-Boltzmann distribution seems most appropriate: instead of the current approach, where the injected carriers have a Maxwellian velocity distribution

$$f(v) \propto \exp \frac{-m^* v^2}{2k_B T} \tag{43}$$

the carriers' velocity distribution are weighted by the perpendicular velocity

$$f(\vec{v}) \propto (\hat{n} \cdot \vec{v}) \exp \frac{-m^* v^2}{2k_B T}, \tag{44}$$

where $\hat{n}$ is the vector normal to the contact. While the pure Maxwell-Boltzmann in eq. 43 does accurately approximate the distributions of velocities of carriers at the ohmic contact, the velocity-weighted Maxwell-Boltzmann distribution in

eq. 44 reflects the fact that, when rather than sampling any electron by the contact, we instead sample only the electrons that cross the contact, electrons with higher velocity normal to the contact cross the contact more often than electrons with lower velocity. This distribution also naturally encodes the fact that electrons crossing the contact have to have a velocity facing into the semiconductor.

Lastly, a major challenge when developing and working with this simulator is the speed at which the simulator runs. IV-sweeps of the devices presented here could take upwards of tens of hours to finish. A big reason for this is the fact that the carriers that contribute to the current flow, that is, the carriers that cross the Schottky barrier, are very few in number, with the vast majority of the simulation time being spent simulating the many carriers in the buffer layer. In [33], [34] a number of methods are described to be able to spend more of the simulation time simulating the "interesting" events and less time simulating the "common" events. The combined phase space ($\vec{r} - \vec{k}$-space) is divided into many regions, separating the "interesting" and "common" events. Each carrier in the system is assigned a weight. By dynamically tracking the number of electrons and the total weight inside each region of phase-space, the electrons are periodically either combined or split to maintain an equal weight in each cell. Depending on the details of which method is used, the splitting and combining events maintain the total momentum, energy, weight, etc. of the system as a whole. By applying such a method, the rare carriers in the depletion region would be split into many carriers, each of low-weight, while the many carriers in the buffer region would be combined into relatively few high-weight electrons. This would in effect let the simulator spend more time recording the behaviour of the "interesting" carriers making up the current flow, spending less time on the "common" carriers in the buffer region which don't provide much mechanism for current flow, effectively shortening the simulation time required to get the same quality of result.

7. Acknowledgements

I would like to thank my supervisor Helena Rodilla for inpsiration and assistance for this work, and Aditya Goturu for many helpful discussions.

Additionally, I would like to thank Vladimir Drakinskiy for providing the measurement data for the diodes simulated in this work, as described in Section 3.3.5.

Lastly, I would like to thank both Agnes Eriksson and the cat that lives in the stairway of my apartment for vital moral support throughout this work.

Bibliography

[1] P. H. Siegel, "THz Instruments for Space," *IEEE Transactions on Antennas and Propagation*, vol. 55, no. 11, pp. 2957–2965, 2007, doi: 10.1109/TAP.2007.908557.

[2] I. Mehdi, J. V. Siles, C. Lee, and E. Schlecht, "THz Diode Technology: Status, Prospects, and Applications," *Proceedings of the IEEE*, vol. 105, no. 6, pp. 990–1007, 2017, doi: 10.1109/JPROC.2017.2650235.

[3] T. Crowe, W. Bishop, D. Porterfield, J. Hesler, and R. Weikle, "Opening the terahertz window with integrated diode circuits," *IEEE Journal of Solid-State Circuits*, vol. 40, no. 10, pp. 2104–2110, 2005, doi: 10.1109/JSSC.2005.854599.

[4] T. Crowe, R. Mattauch, H. Roser, W. Bishop, W. Peatman, and X. Liu, "GaAs Schottky diodes for THz mixing applications," *Proceedings of the IEEE*, vol. 80, no. 11, pp. 1827–1841, 1992, doi: 10.1109/5.175258.

[5] D. P. Santos, "Analysis and Design of Multipliers and Mixers via Monte Carlo Modelling at THz Bands," *Universidad Politécnica de Madrid*, 2014.

[6] H. Hjelmgren, "Numerical modeling of hot electrons in n-GaAs Schottky-barrier diodes," *IEEE Transactions on Electron Devices*, vol. 37, no. 5, pp. 1228–1234, 1990, doi: 10.1109/16.108183.

[7] H. Zirath, "High-frequency noise and current-voltage characteristics of mm-wave platinum n–n$^+$–GaAs Schottky barrier diodes," *Journal of Applied Physics*, vol. 60, no. 4, pp. 1399–1407, 1986, doi: 10.1063/1.337317.

[8] C. Jacobino and P. Lugli, *The Monte Carlo Method for Semiconductor Device Simulation*. Springer-Verlag Wien New York, 1989.

[9] H. Rees, "Calculation of distribution functions by exploiting the stability of the steady state," *Journal of Physics and Chemistry of Solids*, vol. 30, no. 3, pp. 643–655, 1969, doi: 10.1016/0022-3697(69)90018-3.

[10] A. B. W. Fawcett and S. Swain, "Monte Carlo determination of electron transport properties in gallium arsenide," *Journal of Physics and Chemistry of Solids*, vol. 31, no. 9, pp. 1963–1990, 1970, doi: 10.1016/0022-3697(70)90001-6.

[11] C. Jacobino and L. Reggiani, "The Monte Carlo method for the solution of charge transport in semiconductors with applications to covalent materials," *Rev. Mod. Phys.*, vol. 55, no. 3, pp. 645–705, 1983, doi: 10.1103/RevModPhys.55.645.

[12] E. O'Reilly, *Quantum Theory of Solids*. Taylor & Francis e-Library, 2003. doi: 10.1201/9781315273198.

[13] O. Madelung, *Semiconductors: Data Handbook*. Berlin, Heidelberg: Springer Berlin Heidelberg, 2004. doi: 10.1007/978-3-642-18865-7_2.

[14] E. Rhoderick, "Metal-semiconductor contacts," *IEE Proceedings I (Solid-State and Electron Devices)*, vol. 129, no. 1, pp. 1–14, 1982, doi: 10.1049/ip-i-1.1982.0001.

[15] J. A. del Alamo, *Integrated Microelectronic Devices: Physics and Modeling*. Pearson Education, 2017.

[16] M. Fischetti, "Monte Carlo simulation of transport in technologically significant semiconductors of the diamond and zinc-blende structures. I. Homogeneous transport," *IEEE Transactions on Electron Devices*, vol. 38, no. 3, pp. 634–649, 1991, doi: 10.1109/16.75176.

[17] E. M. Conwell and M. O. Vassell, "High-Field Transport in n-Type GaAs", *Phys. Rev.*, vol. 166, no. 3, pp. 797–821, 1968, doi: 10.1103/PhysRev.166.797.

[18] C. Moglestue, *Monte Carlo Simulation of Semiconductor Devices*. Springer Dordrecht, 1993. doi: 10.1007/978-94-015-8133-2.

[19] V. Rideout, "A review of the theory, technology and applications of metal-semiconductor rectifiers," *Thin Solid Films*, vol. 48, no. 3, pp. 261–291, 1978, doi: 10.1016/0040-6090(78)90007-X.

[20] E. H. Rhoderick, "The physics of Schottky barriers," *Journal of Physics D: Applied Physics*, vol. 3, no. 8, p. 1153, Aug. 1970, doi: 10.1088/0022-3727/3/8/203.

[21] A. Y. Tang, "Modelling and Characterisation of Terahertz Planar Schottky Diodes," Doctoral dissertation, 2013.

[22] T.-J. Kim and P. H. Holloway, "Ohmic contacts to GaAs epitaxial layers," *Critical Reviews in Solid State and Materials Sciences*, vol. 22, no. 3, pp. 239–273, 1997, doi: 10.1080/10408439708241262.

[23] U. Ravaioli, "Hierarchy of simulation approaches for hot carrier transport in deep submicron devices," *Semiconductor Science and Technology*, vol. 13, no. 1, p. 1, Jan. 1998, doi: 10.1088/0268-1242/13/1/002.

[24] S. Selberherr, *Analysis and Simulation of Semiconductor Devices*. Springer Vienna, 1984. doi: 10.1007/978-3-7091-8752-4.

[25] J. V. Siles, J. Grajal, and A. Di Carlo, "Design of Submillimeter Schottky Mixers Under Flat-Band Conditions Using an Improved Drift-Diffusion

Model," *IEEE Microwave and Wireless Components Letters*, vol. 19, no. 3, pp. 167–169, 2009, doi: 10.1109/LMWC.2009.2013741.

[26] C. G. Pérez-Moreno and J. Grajal, "Physical Electro-Thermal Model for the Design of Schottky Diode-Based Circuits," *IEEE Transactions on Terahertz Science and Technology*, vol. 4, no. 5, pp. 597–604, 2014, doi: 10.1109/TTHZ.2014.2337655.

[27] J. G. Ruch and G. S. Kino, "Transport Properties of GaAs," *Physical Review*, vol. 174, no. 3, pp. 921–931, Oct. 1968, doi: 10.1103/PhysRev.174.921.

[28] J. Chilleri, Y. Wang, M. S. Shur, and S. K. O'Leary, "An improved empirical model for a semiconductor's velocity-field characteristic applied to gallium arsenide," *Solid State Communications*, vol. 330, p. 114240, 2021, doi: 10.1016/j.ssc.2021.114240.

[29] R. Fauquembergue, J. Zimmermann, A. Kaszynski, E. Constant, and G. Microondes, "Diffusion and the power spectral density and correlation function of velocity fluctuation for electrons in Si and GaAs by Monte Carlo methods," *Journal of Applied Physics*, vol. 51, no. 2, pp. 1065–1071, 1980, doi: 10.1063/1.327713.

[30] T. González and D. Pardo, "Physical models of ohmic contact for Monte Carlo device simulation," *Solid-State Electronics*, vol. 39, no. 4, pp. 555–562, 1996, doi: 10.1016/0038-1101(95)00188-3.

[31] T. G. Sanchez, J. E. V. Perez, P. M. G. Conde, and D. P. Collantes, "Five-valley model for the study of electron transport properties at very high electric fields in GaAs," *Semiconductor Science and Technology*, vol. 6, no. 9, p. 862, Sept. 1991, doi: 10.1088/0268-1242/6/9/005.

[32] D. Moro-Melgar *et al.*, "Monte Carlo Study of 2-D Capacitance Fringing Effects in GaAs Planar Schottky Diodes," *IEEE Transactions on Electron Devices*, vol. 63, no. 10, pp. 3900–3907, 2016, doi: 10.1109/TED.2016.2601341.

[33] M. J. Martín, T. González, D. Pardo, and J. E. Velázquez, "Monte Carlo analysis of a Schottky diode with an automatic space-variable charge algorithm," *Semiconductor Science and Technology*, vol. 11, no. 3, p. 380, Mar. 1996, doi: 10.1088/0268-1242/11/3/017.

[34] C. Wordelman, T. Kwan, and C. Snell, "Comparison of statistical enhancement methods for Monte Carlo semiconductor simulation," *IEEE Transactions on Computer-Aided Design of Integrated Circuits and Systems*, vol. 17, no. 12, pp. 1230–1235, 1998, doi: 10.1109/43.736562.

DEPARTMENT OF MICROTECHNOLOGY AND NANOSCIENCE
CHALMERS UNIVERSITY OF TECHNOLOGY
Gothenburg, Sweden 2026
www.chalmers.se

CHALMERS
UNIVERSITY OF TECHNOLOGY